Muon tagging using a Match-χ^2 based Soft Muon Tagger in top quark analyses using data from the ATLAS detector

Jacobo Ezequiel Blanco

Department of Physics
Royal Holloway, University of London

A thesis submitted to the University of London for the Degree of Doctor of Philosophy

April 26, 2014

DECLARATION

I confirm that the work presented in this thesis is my own. Where information has been derived from other sources, I confirm that this has been indicated in the document. Jacobo Ezequiel Blanco

Abstract

This is an abstract

Contents

List of Figures

List of Tables

Chapter 1

Introduction and motivation

Chapter 2

The Standard Model of Particle Physics

Particle physics, or high-energy physics, is the study of the most fundamental consituents of matter and their interactions. The best current description of these interactions is known as The Standard Model of Particle Physics (SM); a group of theories that cover all currently known particles and their interactions. The SM was developed through-out the latter half of the 20th century and has seen tremendous success in predicting the behaviour of our universe at the most fundamental level. The SM has stood the test of time and rigorous examination by numerous experiments. Additionally many of its parameters have been measured with tremendous precision e.g.the electron magnetic moment g is known to 10^{-13} [2]. The last piece to be confirmed was the existence of the Higgs boson, which in turn points to the existence of the so-called Higgs field. Evidence of the elusive Higgs were observed by the ATLAS and CMS experiments at CERN [3,4]. Despite its tremendous success, the SM cannot account and explain for all observed phenomenon in the universe. Firstly, the theory requires many of its parameters to be measured empirically. The theory does not a priori provide a value for these parameters such as the number of particle generations. Additionally the theory does not describe the most familiar of the forces, gravity. Furthermore, the SM does not provide a candidate for dark matter, which is believed to make up more than 80% of the total matter in the universe. The asymmetry between matter and antimatter is also not fully explained by the SM. As such there is a strong focus on developing theories which go beyond the standard model (BSM) to provide an answer to these open questions. The discussion in this chapter is largely based on [5] and [6].

The SM describes the nature of the interactions of the fundamental constituents of our universe in terms of the three different fundamental forces: strong, weak and electromagnetic each described by a specific theory. As mentioned before, the most familiar of the forces, gravity, is not described by the SM. The SM classifies particles into several categories depending on their properties and allowed interactions. Particles which have a half-integer spins (e.g. $S = \frac{1}{2}$, $\frac{3}{2}$,...) are known as *fermions*, these are the basic constituents of matter. Particles with integer spins (e.g. S =0, 1,...) are known as *bosons*, these mediate interactions between fermions and other bosons.

Fermions can be divided into two subgroups: quarks, which can interact via the strong, weak and electromagnetic forces and leptons which can only interact by the weak and electromagnetic forces. There are six known leptons: electron e, muon μ and tau τ, which all have electric charge[1] $Q = 1$, and the corresponding electrically neutral neutrino ν_e, ν_μ and ν_τ. Analogously, six quark *flavours* are known: u, c and t, with electric charge $Q = +2/3$ and d, s and b, with electric charge $Q = -1/3$.

Quarks and leptons are divided into three generations, which differ only by the mass and flavour of their constituent fermions, each generation being heavier then the previous. A summary of all elementary particles described by the SM can be found in Table 2.1.

For every matter fermion (f) there is an equivalent antimatter partner ($\bar{f}$) which possesses the same characteristics as its matter companion but is opposite in electric charge. Thus 12 matter particles are combined with 12 antimatter partners for a total of 24 elementary particles which form all visible matter in the universe.

The interaction between fermions occur via the exchange of spin one particles known as bosons. Each force is mediated by one or more bosons (Table 2.2). The strong force is mediated by a set of massless bosons known as the gluons. The weak force is mediated by a neutral massive boson known as the Z boson and a pair of charged massive bosons known as the W bosons. Finally, the elecromagentic force is mediated by a massless

[1] The electric charge is always state in units of elementary charge e

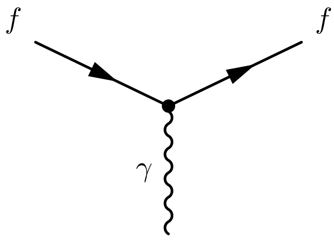

Figure 2.1: The interaction vertex described by QED. One can obtain all possible vertex shapes by rotating this basic vertex and assigning the appropriate electric charge and making sure to conserve lepton number across the vertex.

boson known as the photon. Note that each boson has an antimatter partner however some are indistinguishable from their matter partner. A summary of their properties is shown in Table 2.1.

Each fermion has a set of so-called quantum numbers which dictate the type of interactions that can occur. For example each lepton has a lepton number associated with it, electrons have an electron lepton number (L_e) of $+1$, while the positron has $L_e = -1$. Muons and taus have their own respective lepton number (L_μ and L_τ). Each neutrino has lepton number $L_f = 1$ and their anti-matter counterpart have $L_f = -1$. Each of these lepton numbers is conserved separately across interaction vertices. Another example of a quantum number is baryon number (B), each quark has $B = \frac{1}{3}$ and anti-quarks have $B = -\frac{1}{3}$.

2.1 Quantum Electrodynamics

The interaction of particles via the electromagnetic force is described by Quantum Electrodynamics or QED. These interactions are mediated by the massless neutral boson known as the photon and the strenght of the interaction is characterized by the fine-structure constant α. All electrically charged fermions are allowed to interact, since the photon itself is not charged, no self-interaction is allowed within QED. Figure 2.1 shows the single vertex described by QED, where two fermions interact via a photon. Note that the electric charge is conserved across the vertex, so for example $\gamma \to e^+e^+$ is not allowed within QED.

By combining different forms of this vertex one can build every possible QED interaction. For example an e^+e^- pair can annihilate to create energy in the form of a

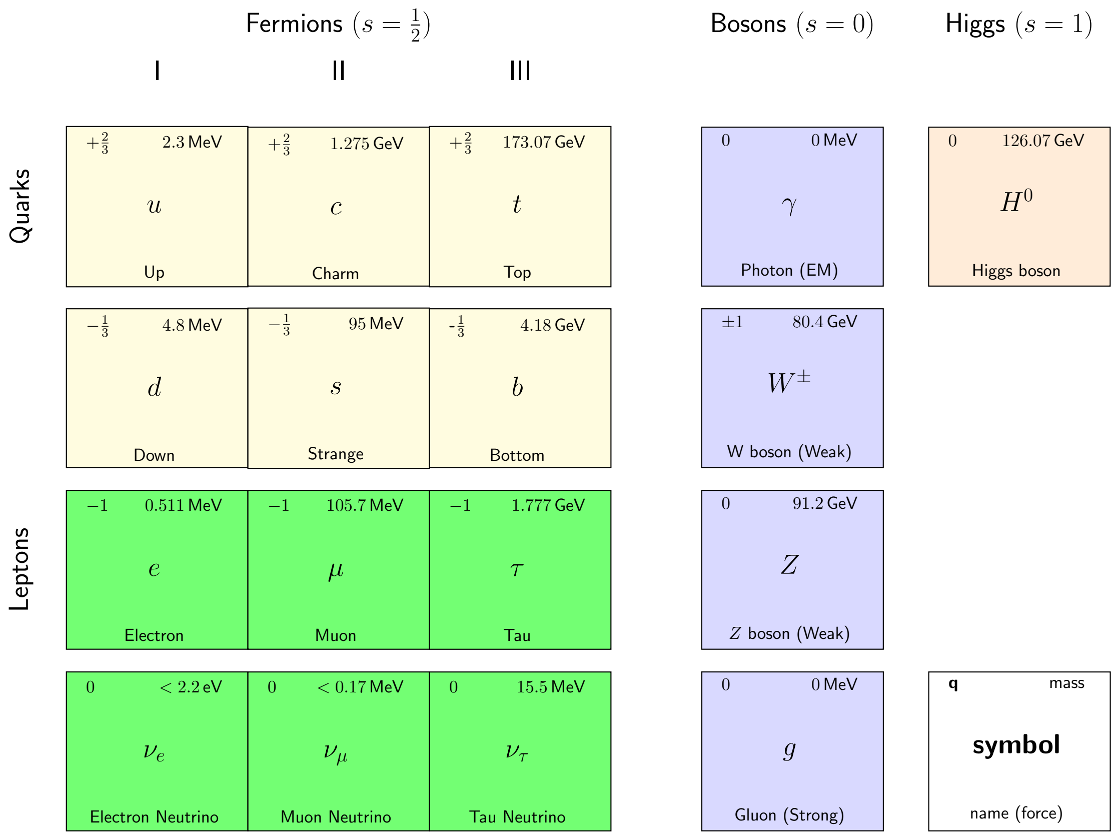

Table 2.1: A summary of all elementary particles described by the SM [1]. Note the various groupings and divisions including by spin, generation and particle type. Within the fermion sector the quarks are shown in yellow and the leptons are shown in green. These are grouped into three different generations traditionally denoted by roman numerals. The force mediators known as gauge bosons are shown in blue and finally the recently discovered Higgs boson with a spin of zero.

Name	Relative Strength	Boson
Strong	10^{38}	Gluons
Electromagnetic	10^{36}	Photon
Weak	10^{25}	$W^{\pm}$and Z^0
Gravity	1	Graviton*

Table 2.2: A summary of the four fundamental forces ordered by relative strength. These are approximate relative strengths for the purpose of demonstrating the hierarchy of forces as a function of their strength. A more accurate determination of the interaction strength depends on the details of the interaction itself. Note however the order-of-magnitude differences in the relative strengths of these forces. Note that the graviton is the theoretical boson responsible for mediating gravitational interactions, it is not part of the SM.

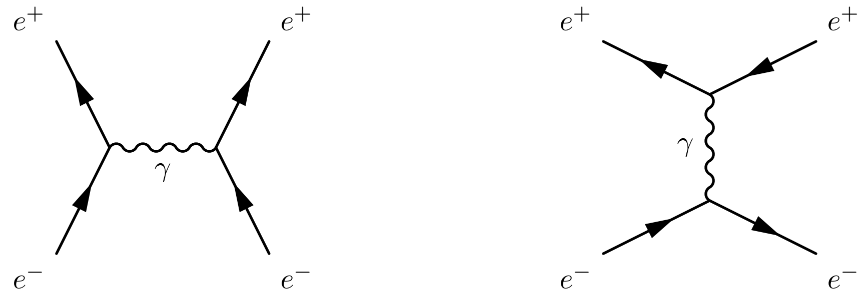

(a) Electron-Positron pair annihilation mediated by a photon.

(b) Electron-Positron pair scattering via the emission of a photon.

Figure 2.2: Feynman diagrams of the process $e^+e^- \rightarrow e^+e^-$ allowed in QED. Note that these are the simplest diagrams, also known as tree level diagrams, and additional vertices can be added to produce higher-order diagrams of the same process.

photon as shown in Fig. 2.2a and then subsequently decay into an additional e^+e^- pair. Electrons can scatter by emitting a photon which is then absorbed by a positron as shown in Fig. 2.2b this processis known as Bhabha scattering.

2.2 Quantum Chromodynamics

Interactions via the strong force are described in the theory of Quantum Chromodynamics or QCD. These interactions are mediated by a set of massless neutral bosons known as gluons. QCD introduces the concept of colour, which similarly to electrical charge, determines the possible interactions that can occur via the strong force. Colour can take three states: red (antired), blue (antiblue), green (antigreen):

For example both quarks and gluons possess colour and as a result gluons, unlike photons, can self-interact in a three gluon vertex (Figure 2.3c) or a four gluon vertex (Figure 2.3b). As with electrical charge, colour-charge must also be conserved. Thus in the scattering process $q \rightarrow q + g$ shown in Figure 2.3a the flavour of the quark may not change but the colour-charge does and the gluon carries away the difference in colour. Thus each gluon has two color charges associated it. Naively one would expect nine different types of gluon that participate in interaction, owing to the nine possible combinations of colour and anticolour, however the SU(3) symmetry on which QCD is based results in a colour octet:

$$\begin{array}{cc}
(r\bar{b} + b\bar{r})/\sqrt{2} & -i(r\bar{g} - g\bar{r})/\sqrt{2} \\
-i(r\bar{b} - b\bar{r})/\sqrt{2} & (b\bar{g} + g\bar{b})/\sqrt{2} \\
(r\bar{r} + b\bar{b})/\sqrt{2} & -i(b\bar{g} - g\bar{b})/\sqrt{2} \\
(r\bar{g} + g\bar{r})/\sqrt{2} & (r\bar{r} + b\bar{b} - 2g\bar{g})/\sqrt{6}
\end{array}$$

and a "colour singlet":

$$(r\bar{r} + g\bar{g} + b\bar{b})/\sqrt{3} \tag{2.1}$$

which is overall colourless.

There are then eight different gluons that can participate in QCD interactions each with a different colour-charge combination. Additionally there is a ninth combination which is overall colorless so it cannot take part in interactions.

In an analogous fashion to screening which occurs with electric charges, quark-antiquark pairs act like dipoles which screen the true colour charge of the central quark. However since gluons also carry colour, they cause the opposite effect (anti-screening) to amplify and change the observed colour of the quark. Which effect wins out depends on the number of colours in the theory and the number of quark flavours. As it is with three colour states and six different quark flavours, anti-screening is the overall dominant effect. As a result the colour potential decreases with distance and quarks experience very little potential when very near to each other. This effect is known as asymptotic freedom and results in quarks only existing within colorless bound states known as *hadrons*.

Hadrons can be divided into two categories: *mesons*, which contain a quark and an antiquark ($q\bar{q}$); and *baryons* which are made of three quarks (or antiquarks) each with a different (anti)colour-charge to result in a colourless composite particle. Common examples of baryons are protons (uud) and neutrons (udd) which are the building blocks of atomic nuclei. While π^0 ($u\bar{u}/d\bar{d}$) is a commonly produced meson in hadron colliders. Note that due to the quark configuration, baryons have baryon number $B = +1$ while mesons have $B = 0$.

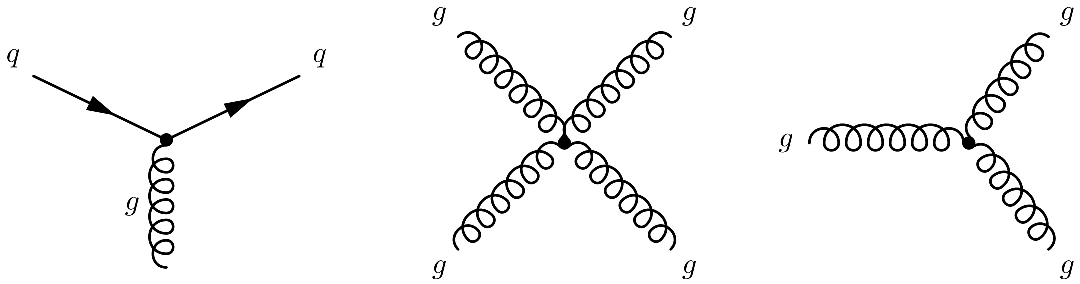

(a) Quark-gluon vertex.

(b) Four-gluon vertex

(c) Three-gluon vertex

Figure 2.3: Diagrams of the fundamental interaction vertices described by quantum chromodynamics.

2.3 Weak Interactions

The final type of interaction involves the so-called weak force. The weak force is responsible for β^- decay ($n \rightarrow p + e^- + \overline{\nu}_e$) and β^+ decay. Interactions via the weak force are mediated by a single neutral massive boson and two charged massive bosons. Since the bosons responsible for weak interactions are massive, the range of interaction is very short, unlike electromagnetic interactions via a massless photon.

All fermions can take part in interactions via the weak force. Let us consider weak interactions involving only leptons. The weak neutral vertex is very similar to the basic vertex seen in QED (2.1) A valid interactions via the weak force is then formed by combining these simple vertices (Figure 2.4) while taking care to conserve electric charge and lepton flavour. An example of a leptonic weak interaction is muon decay ($\mu \rightarrow \nu_\mu W^- \rightarrow \nu_\mu e^- \overline{\nu}_e$) shown in Figure 2.5.

Let us consider weak interactions involving quarks. The neutral vertex is similar to that of the leptonic version, a quark can emit a Z boson or a Z boson can decay forming a quark-antiquark pair. The charged current then changes the flavour of an up-type quark into a down-type quark (or vice-versa) with a W boson of the appropriate charge (Figure 2.4c). It is possible for a weak interaction to change the flavour of a quark across families. A well known example of such an interaction is Kaon decay ($K^+ \rightarrow \mu^+ \nu_\mu$). In order to account for this interaction and preserve the universality of weak interactions, Nicola Cabibbo postulated [7] that the states that the states that couple to the charged

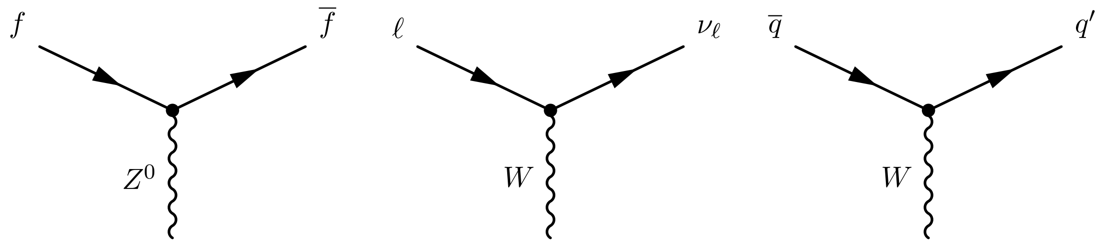

(a) Neutral current weak vertex (b) Charged current vertex involving leptons (c) Charged current vertex involving quarks

Figure 2.4: The neutral current and charged current vertices allowed via the weak force. Where f can be an e, μ or τ and ν_ℓ is the corresponding lepton neutrino of the same flavour. One can obtain all possible interaction vertices by rotating these basic vertices and assigning the appropriate electric charge and making sure to conserve lepton flavour across the vertex.

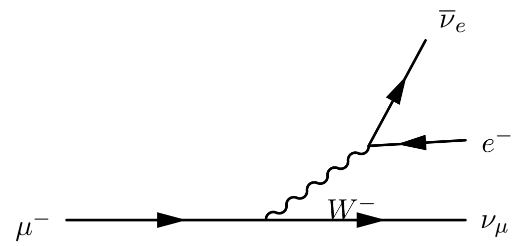

Figure 2.5: Neutral current weak scattering vertex

current are really a mixture of 'rotated' quark states:

$$\begin{pmatrix} u \\ d' \end{pmatrix} \begin{pmatrix} c \\ s' \end{pmatrix} \tag{2.2}$$

where

$$d' = d\cos\theta_c + s\sin\theta_c \tag{2.3a}$$

$$s' = -d\sin\theta_c + s\cos\theta_c \tag{2.3b}$$

This introduces an arbitrary parameter into the theory known as the quark mixing angle or the Cabibbo angle, named after Nicola Cabibbo who developed the phenomenon of quark mixing. The introduction of quark mixing has the effect of attenuating the interaction strength at vertices involving multiple quark generations. Interactions which cross one generation are said to be Cabibbo Suppressed while those that cross two generations are Doubly Cabibbo suppressed.

Taking into account the three quark generations, quark mixing can be expressed in matrix notation as shown in Equation 2.4. This unitary matrix is known as the Cabibbo-Kobayashi-Maskawa Matrix (CKM Matrix) after Cabibbo which initially postulated quark mixing and Makoto Kobayashi and Toshihide Maskawa who later added an additional generation, containing the top and bottom quarks, to the matrix [8].

$$\begin{pmatrix} d' \\ s' \\ b' \end{pmatrix} = V_{CKM} \begin{pmatrix} d \\ s \\ b \end{pmatrix} = \begin{pmatrix} V_{ud} & V_{us} & V_{ub} \\ V_{cd} & V_{cs} & V_{cb} \\ V_{td} & V_{ts} & V_{tb} \end{pmatrix} \begin{pmatrix} d \\ s \\ b \end{pmatrix} \tag{2.4}$$

Several parameterizations of the CKM matrix exist, the "standard" parametrization uses angles θ_{12}, θ_{23}, θ_{13} and a phase δ_{13}:

$$V_{CKM} = \begin{pmatrix} c_{12}c_{13} & s_{12}c_{13} & s_{13}\exp(-i\delta) \\ -s_{12}c_{23} - c_{12}s_{23}s_{13}\exp(i\delta) & c_{12}c_{23} - s_{12}s_{23}s_{13}\exp(i\delta) & s_{23}c_{13} \\ s_{12}s_{23} - c_{12}c_{23}s_{13}\exp(i\delta) & -c_{12}s_{23} - s_{12}c_{23}s_{13}\exp(i\delta) & c_{23}c_{13} \end{pmatrix} \tag{2.5}$$

where $c_{ij} = \cos\theta_{ij}$ and $s_{ij} = \sin\theta_{ij}$ for i=1,2,3. This parametrization has the advantage that each angle θ_{ij} relates to a specific transition from one generation to the other. If $\theta_{13} = \theta_{23} = 0$ the third generation is not coupled to the other two and the matrix reduces to the original matrix postulated by Cabibbo. Note that θ_{12} is the Cabibbo angle, θ_c, described earlier.

Another parameterization due to Wolfenstein [9] expresses all elements in terms of the Cabibbo angle by defining $\lambda \equiv s_{12} = \sin\theta_{12}$ and then expressing the other elements in terms of powers of λ:

$$V_{CKM} \approx \begin{pmatrix} 1-\lambda^2/2 & \lambda & A\lambda^3(\rho - i\eta) \\ -\lambda & 1-\lambda^2/2 & A\lambda^2 \\ A\lambda^3(1-\rho-i\eta) & -A\lambda^2 & 1 \end{pmatrix} \tag{2.6}$$

where A, ρ and η are all real numbers intended to express the order of magnitude differences between s_{12} and the other elements in the matrix. Of course, all the elements should be the same irrespective of which parametrization is used.

The elements of the CKM matrix have been measured and the latest accepted results are summarized in 2.8 [1]. The interaction strength is then proportional to $|V_{ij}|^2$. Including all three generations the sum of all possible transitions from a given quark, q, is unity:

$$\sum |V_{qi}|^2 = 1 \tag{2.7}$$

Note that the term V_{tb} is approximately unity and by far dominates over the other V_{tj} terms. This means that the top-quark transitions almost exclusively into a b-quark ($t \to Wb$) with transitions $t \to Ws$ and $t \to Wd$ being exceedingly rare. The soft muon tagger which is the focus of this thesis relies on weak semileptonic decays of b-quarks. From 2.8 one can see that the transition $b \to c$ dominates over $b \to u$. Additionally the focus of this theses is on semileptonic $t\bar{t}$ events, where one of the W bosons in the event decays to quarks as per the magnitude of V_{ij}.

$$V_{CKM} = \begin{pmatrix} 0.97427 \pm 0.00015 & 0.22534 \pm 0.00065 & 0.00351^{+0.00015}_{-0.00014} \\ 0.22520 \pm 0.00065 & 0.97344 \pm 0.00016 & 0.0412^{+0.0011}_{-0.0005} \\ 0.00867^{+0.00029}_{-0.00031} & 0.0404^{+0.0011}_{-0.0005} & 0.999146^{+0.000021}_{-0.000046} \end{pmatrix} \tag{2.8}$$

An additional unique feature of weak interactions is that the charge conjugation-parity (CP) symmetry is violated. The operator C denotes the change of a particle by its antiparticle partner and P denotes a reversal of helicity (the projection of spin onto the momentum of a particle). A clear violation of C and P was observed in the radioactive decay of Cobalt-60, where the resulting electrons were preferentially emitted in the opposite direction of the nuclear spin of the Cobalt. Thus weak currents only couple to left-handed neutrinos (or right-handed antineutrinos) this is then a violation of parity. Additionally charge symmetry is also violated since a left-handed neutrino is preferentially picked over a left-handed antineutrino. Finally in 1964 CP violation was observed in the decay of neutral kaon.

Thus the probability of $\overline{a} \to \overline{b}$ is not equal to that of $a \to b$. The existence of CP violation has interesting consequences for the formation of the early universe. The preferential production of matter over antimattter in CP violating interactions would shift the balance in favour of matter resulting in a universe similar to our own. Finally as with QCD, weak interactions couple weak bosons to each other. Thus the vertex $Z \to W^-W^+$ is allowed via the weak force.

2.3.1 Electroweak Unification and the Higgs mechanism

The unification of the electromagnetic and weak theories was first proposed by Glashow and later developed by Weinberg and Salam into the electroweak theory. The theory postulates that while at low energies the two forces are to be treated separately, at higher the two can be seen as a single force. Thus the two forces are different manifestation of the same "electroweak" interaction. There were several stumbling blocks to the unification of the forces. Firstly, the boson which drives the electromagnetic interaction, the photon, is massless while the weak bosons are both massive. Evidence for the massive nature of these bosons has been established by experimental results from at CERN.

Thus the symmetry of the theory must be spontenously broken in some way. A mechanism for ElectroWeak Symmetry Breaking (EWSB) was postulated by Higgs, Brout, Englert and others which introduces massess to the weak bosons and posits the existence of an additional scalar (spin $S = 0$) boson known as the Higgs boson.

Gauge Theories

Gauge invariance is one of the underlying invariances which underpins the Standard Model. Given the so-called Dirac lagrangian[2]

$$\mathcal{L} = i\hbar c\overline{\psi}\gamma^\mu\partial_\mu\psi - mc^2\overline{\psi}\psi \tag{2.9}$$

which describes a free particle of spin-$\frac{1}{2}$ with mass m. Note that it is invariant under the transformation

$$\psi \to e^{i\theta}\psi, \text{ where } \theta \text{ is a real number} \tag{2.10}$$

[2]A Lagrangian is a mathematical function that describes the underlying dynamics of a system as a function of time and space coordinates (x^μ) and their time derivatives.

since the adjoint $\overline{\psi} \rightarrow e^{-i\theta}\overline{\psi}$ and the two terms cancel out. This is known as a *(global) gauge transformation.* This is essentially a phase transformation which is constant everywhere. Meaning the phase change is the same in all points of space-time. A "local" gauge transformation occurs when the phase is different for different points in space-time:

$$\psi \rightarrow e^{i\theta(x)}\psi \tag{2.11}$$

Note that the Dirac lagrangian (Equation 2.9) is then not invariant under a local gauge transformation since extra terms are created by the derivative. This then implies that the underlying physics of such a theory depends ones position in space-time. Thus local gauge invariance must be imposed. In the case of the Dirac lagrangian, this is done by introducing additional terms to the Dirac lagrangian which will cancel the extra terms introduced by the local gauge transformation. As it turns out this results in the introduction of a new massless vector field that couples to ψ.

The new lagrangian then describes a spin-$\frac{1}{2}$ particle with mass m that interacts with a free massless field. This new field can be indentified as the electromagnetic field and the spin-$\frac{1}{2}$ particles are electrons and positrons. Thus the resulting lagrangian describes all interactions that form part of quantum electrodynamics.

A similar procedure can be applied to the color quark model and obtain a description of all QCD interactions. However requiring that the weak theory be a gauge theory (invariant under local gauge transformation) encounters a problem since the weak bosons are known to be massive. There must be some mechanism via which the $W^{\pm}$ and Z^0 obtain mass.

The Higgs mechanism posits the existence of a complex scalar field doublet that when introduced into the electroweak Lagrangian results in the weak fields acquiring a mass term. In other words the $W^{\pm}$ and Z^0 interact with the Higgs field and obtain a mass. An additional consequence of introducing the Higgs field is the inclusion of a scalar boson particle, the the so-called "Higgs boson". Finally the Higgs field also couples to fermions via the Yukawa coupling generating gauge invariant mass terms for the fermions as well.[3].

[3]For a more complete description of the mathematical procedure see [6].

The SM Lagrangian in its current form including the Higgs potential is shown in Equation 2.12. This expression describes all possible particle interactions that form part of the SM, of particular interest are the fermion mass term which couples the fermion field (ψ) to the scalar Higgs field (ϕ) and the Higgs kinetic and potential terms.

$$\begin{aligned}\mathcal{L} = & \underbrace{-\frac{1}{4}W^a_{\mu\nu}W^{\mu\nu a}}_{\text{Weak Field}} \underbrace{-\frac{1}{4}B_{\mu\nu}B^{\mu\nu}}_{\text{EM Field}} \underbrace{-\frac{1}{4}G^a_{\mu\nu}G^{\mu\nu a}}_{\text{Strong Field}} \\ & + \underbrace{\overline{\psi}\not{D}_\mu\psi}_{\text{Fermion Kinetic}} + \underbrace{\lambda\overline{\psi}\psi\phi}_{\text{Fermion Mass}} \\ & + \underbrace{|D_\mu\phi^2|}_{\text{Higgs Kinetic}} - \underbrace{V(\phi)}_{\text{Higgs Potential}}\end{aligned} \tag{2.12}$$

Chapter 3

Top-quark physics

The third generation of quarks was first proposed by Kobayashi and Maskawa in a paper published in 1973 [8] as a way to exaplain the CP violation observed in Kaon decays. The existence of the third generation was confirmed when the lighter of the two constituents, the b quark, was discovered in 1977 [10].

Due to its large mass, direct confirmation of the existence of the top quark required the construction of very powerful accelerators. The top quark was discovered by the CDF and D0 experiments at Fermilab in 1995 [11, 12].

Its large mass makes the top quark a very interesting object of study. The current world average for the mass of the top is $m_t = 173.07 \pm 0.52 \pm 0.72$ GeV based on results from Tevatron and the LHC [1]. Due to its mass the top quark has an extremely short lifetime $\tau \approx 0.5 \times 10^{-24}$ s, too short to interact via the strong force and hadronize into a bound state [13]. Instead the top quark decays weakly producing a W boson and a b quark almost exclusively. This allows experimentalist to directly study the properties of a bare quark. An impossibility with the other quarks which bind with other quarks to form hadrons. Measurement of top quark properties (mass, charge, forward-backward asymmetry, couplings, etc...) forms a large part of high energy physics research. Measurement of these properties provide rigorous tests of the SM, point towards the existence of new physics or exclude some BSM theories.

From an experimental perspective, top quark decays can produce a very interesting signature which includes leptons, jets and missing energy due to the escaping neutrino[1].

[1] Neutrinos do not interact with the detector material and thus escape without being detected

The study of top quark decays relies on all parts of a general purpose detector such as ATLAS or CMS. In additional $t\bar{t}$ pair production constitutes a background for many other SM and BSM searches, as such understanding this process well is fundamental for almost all areas of HEP research.

3.1 Top quark production

Top quarks can be produced in two manners, single top production and $t\bar{t}$ pair production. In hadron colliders production dominantly takes place via the strong force through $qq \rightarrow t\bar{t}$ and $gg \rightarrow t\bar{t}$ at leading order. The feynman diagrams for these interactions are shown in Figure 3.1.

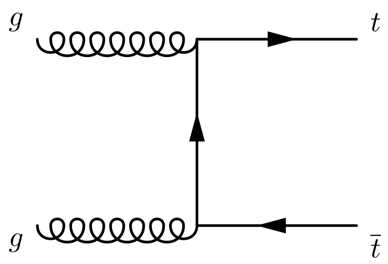

(a) Gluon fusion (t-channel)

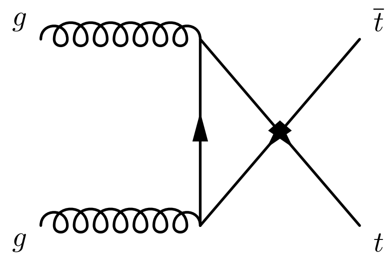

(b) Gluon fusion (u-channel)

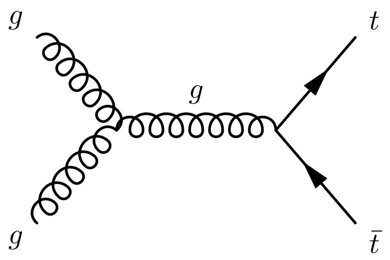

(c) Gluon fusion (s-channel)

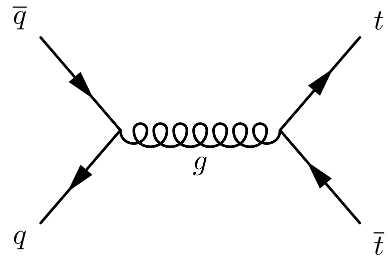

(d) Quark pair annihilation

Figure 3.1: The leading order Feynman diagrams for $t\bar{t}$ production.

Single top production occurs via the weak force almost exclusively through the Wtb vertex. The leading order weak interactions are shown in Figure 3.2. As top quark pair production can proceed via the strong force it occurs overwhelmingly more often than single top production.

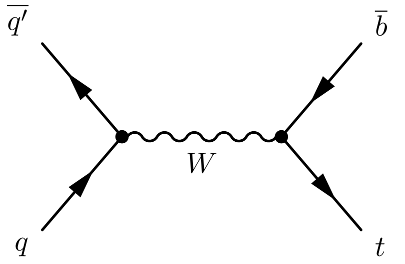

(a) s-channel

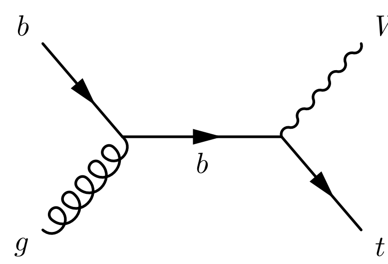

(b) tW-channel

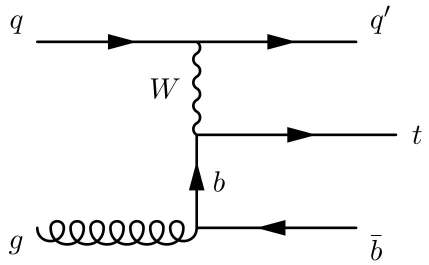

(c) Associated with a q and $\bar{b}$

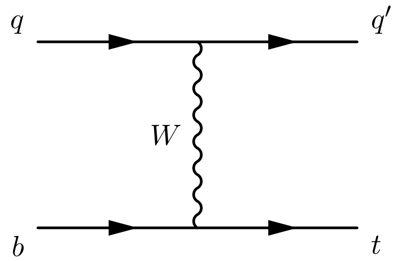

(d) Associated with a q

Figure 3.2: Example Feynman diagrams for single top quark at leading order.

3.2 Top quark decay modes

The top quark decays almost exclusively into a W boson and a b-quark. The ratio of branching ratios $\Gamma(t \to Wb)/\Gamma(t \to Wq(q = b, s, d))$ is 0.91 ± 0.04 [1].

As the LHC collides proton-proton beams, the overwhelming majority of events produced will feature multiple hadronic *jets*, a stream of particles resulting from the hadronization of quarks in the detector, most of which will originate from "light" quarks[2]. Unlike these light quarks, b quarks leave a distinct signature in the detector as they travel a certain distance within a B hadron before producing a jet. Additional features such as the semi-leptonic decay of b quarks can be exploited to determine the presence of such a quark in the detector. Collectively analysis techniques that permit the detection of b-jets are known as *b-tagging*. Top quark events will produce two b quarks, making b-tagging techniques a central part of any $t\bar{t}$ analysis.

The other part of the top decay, the W boson is used to classify $t\bar{t}$ events. As discussed in Section 2, W bosons can decay leptonically ($\ell\nu_\ell$) or hadronically ($W \to q\bar{q}'$) driven by the CKM vertex element, since $\Gamma \propto |V_{ij}|^2$. The various branching ratios of W

[2] The term light quarks usually refers to quarks in the first two generations. Light jets are those originating from those quarks

Decay	Branching ratio
$W \rightarrow e + \nu$	$(10.75 \pm 0.13)\%$
$W \rightarrow \mu + \nu$	$(10.57 \pm 0.15)\%$
$W \rightarrow \tau + \nu$	$(11.25 \pm 0.20)\%$
hadrons	$(67.60 \pm 0.27)\%$

Table 3.1: Branching ratios for the decay of W boson. Note that the "hadrons" refers to a possible combination of $q\bar{q}'$ where $\bar{q}'$ denotes the antiquark of a flavour different to that of the first quark.

decays are presented in Table 3.1.

Thus $t\bar{t}$ events are labelled as "dilepton", "all-hadronic" or "lepton + jets" depending on the combination of W decays present. The probability for $t\bar{t}$ event to be of a given type is dependent on the branching-ratios of W decays shown a priori. As can be seen from Figure 3.3 the all-hadronic events dominate, followed by the lepton plus jets and dilepton. Each of these types requires a very different analysis approach due to their distinct backgrounds, branching-ratio, detector signature and reconstruction requirements.

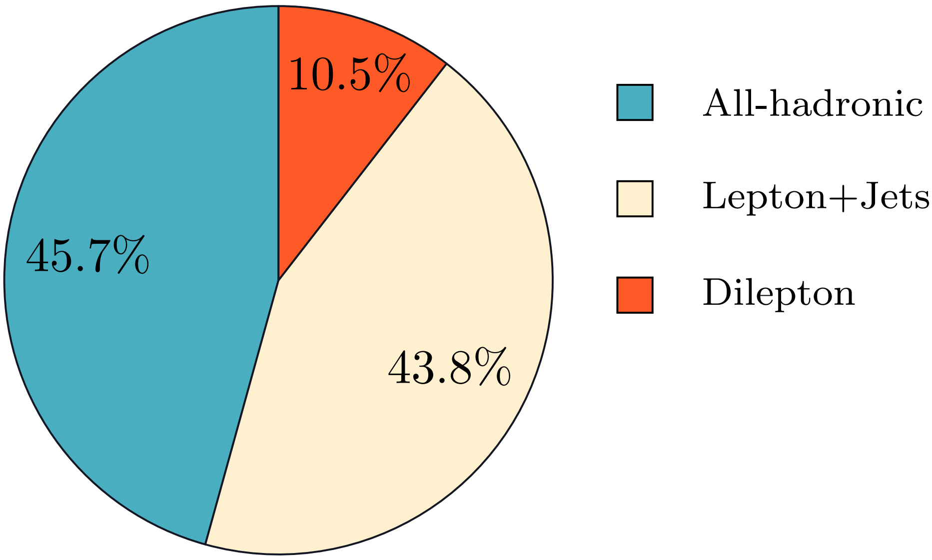

Figure 3.3: Branching ratios of all possible $t\bar{t}$ decays. These probabilities are based on the branching-ratios of W decay shown in Table 3.1.

The all-hadronic final state includes four light quarks which will hadronize to form four Light Flavour (LF) jets and two b quarks leading to two b jets. Due to the large hadronic activity the all-hadronic channel is very challenging. As mentioned before, hadronic collisions produce events with a large number of quarks – and thus jets – in the final state. The background to the all-hadronic channel are therefore very high. As shown in Figure 3.3, the all-hadronic channel has the largest branching ratio of the three.

The dilepton final state includes two leptons, large missing energy from two neutrinos which escape the detector and two b jets. In constrast to the all-hadronic channel, dilepton events are very clean due to the presence of leptons and missing energy, however the branching ratio is very small and reconstruction of the top is challenging do the presence of two neutrinos which escape the detector without interacting.

Finally, the lepton plus jets channel has a large branching ratio while having a distinct signature with an isolated lepton[3] and missing energy as well as LF and b jets. Typical lepton plus jets are shown in Note that leptons in this case refers to e and μ and excludes the τ. The τ lepton is unstable and sufficiently heavy to decay haronically via the weak force producing two quarks, losing the advantageous distinct signature of a lepton plus jets event. An example of the full lepton plus jets chain is shown in Figure 3.5.

3.2.1 Motivations for selecting the ℓ+jets channel

Due to its distinct signature and high branching ratio the lepton plus jets channel was chosen as the focus for the analyses presented in this thesis. Additionally the presence of only one neutrino allows for a reconstruction of the mass of the leptonic top (the top whose associated W decays leptonically) in the transverse plane and a full mass reconstruction of the top mass on the hadronic side[4].

3.3 Latest developments in top physics

This section discusses a few of the latest measurements in the area of top quark pair production with a focus on LHC results.

As discussed top quark decays provide the only probe to study the properties of a bare quark. Measurements of its properties provide a stringent test of the SM and could show hints of new physics from BSM theories. Moreover due to its final state signature,

[3] A lepton produced far from other physics objects (jets, leptons, etc...)

[4] The methods used for this mass reconstruction is complex and not discussed in this thesis

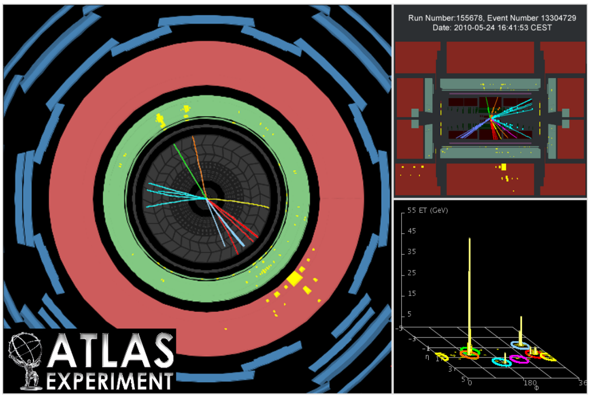

(a) caption

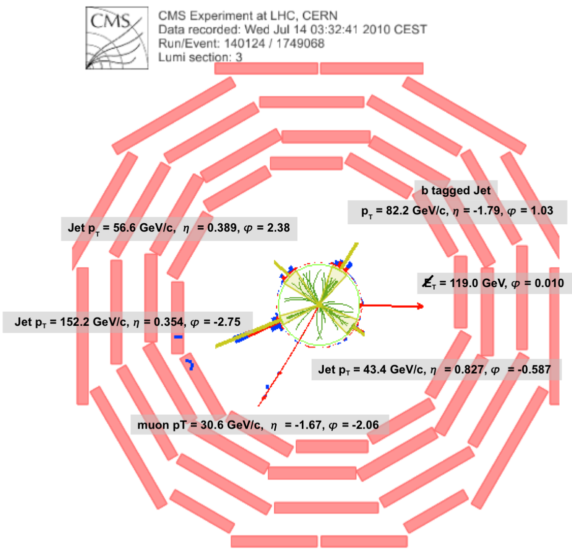

(b) caption

Figure 3.4: Transverse event displays of ℓ+jets events at (a) ATLAS and (b).

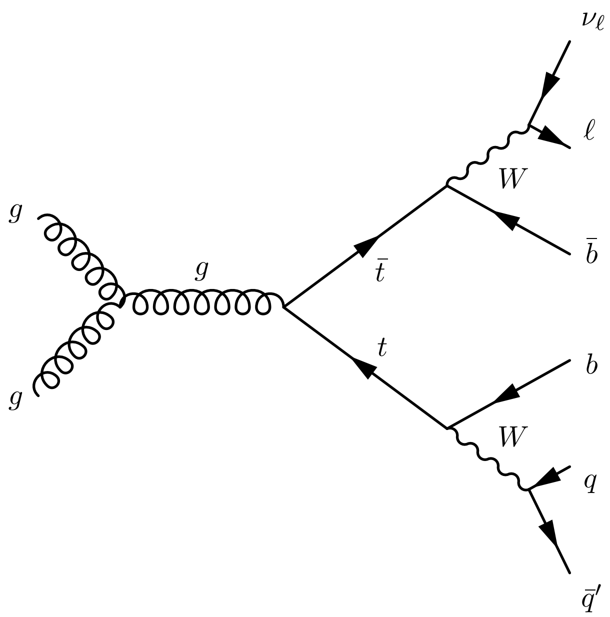

Figure 3.5: The feynman diagram of lepton plus jets channel including $t\bar{t}$ production via gluon fusion and decay with a leptonically decaying W^+. Note that all other production mechanisms are also considered and the final state where the W^- is decayed leptonically is also taken into account.

top quark pair production particularly in the lepton + jets channel, form the background to many searches for new physics. Additionally all parts of the detector are utilized in the reconstruction of ℓ+jets events and as such it is possible to use these events to tune or *calibrate* many analysis and reconstruction techniques.

Cross-section measurement

Measurement of the cross-section of the top quark is a benchmark test of the SM. Any statistically significant deviation from the predicted value could point to the presence of new physics. Some BSM theories posit the existence of particles which could decay to produce a $t\bar{t}$ pair. If such theory is correct this would be observed in an increase in the cross section measured away from the predicted SM value.

Experimentally measurement of the cross-section is vital when attempting to reduce and estimate the amount of top quark background present in other analyses. Searches for the Higgs boson, exploit many different channels, many of which include $t\bar{t}$ events as a background. The type of events predicted by the BSM theory, Supersymmetry (SUSY) include a large amount of missing energy, leptons and jets in the final state. Top quark pair events mimmick these processes and constitute a large background.

A summary of all $t\bar{t}$ cross section measurements from the LHC is shown in Figure 3.6 and a comparison against the Tevatron measurement at $\sqrt{s} = 1.96$ TeV is shown in Figure 3.7.

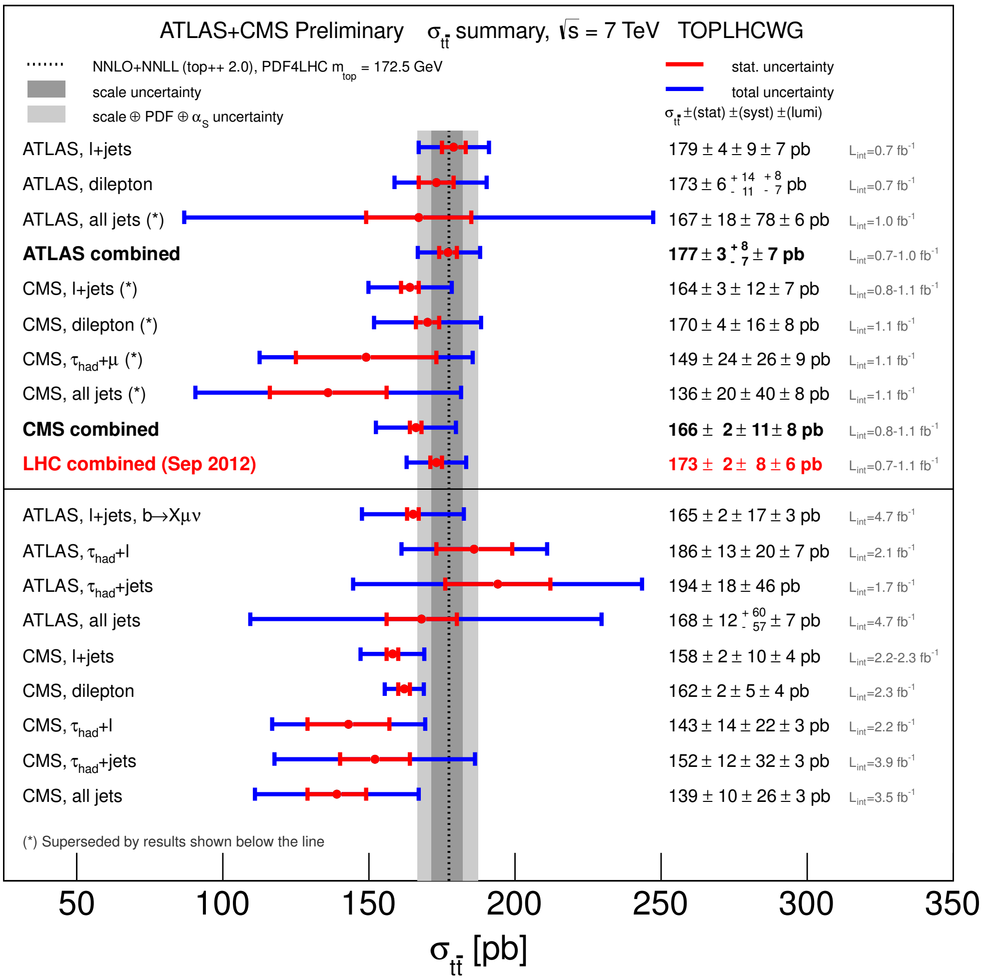

Figure 3.6: A summary of all $t\bar{t}$ production cross section measurements performed at the LHC at $\sqrt{s} = 7$ TeV. Note the theory prediction shown as a dotted black line with its associated uncertainties as grey bands. The results shown above the black line have been statistically combined, producing the results labelled as **combined**. Many of these analyses have been superseded and the results are shown below the line. Other analyses performed but not included in the combination are also shown below the line.

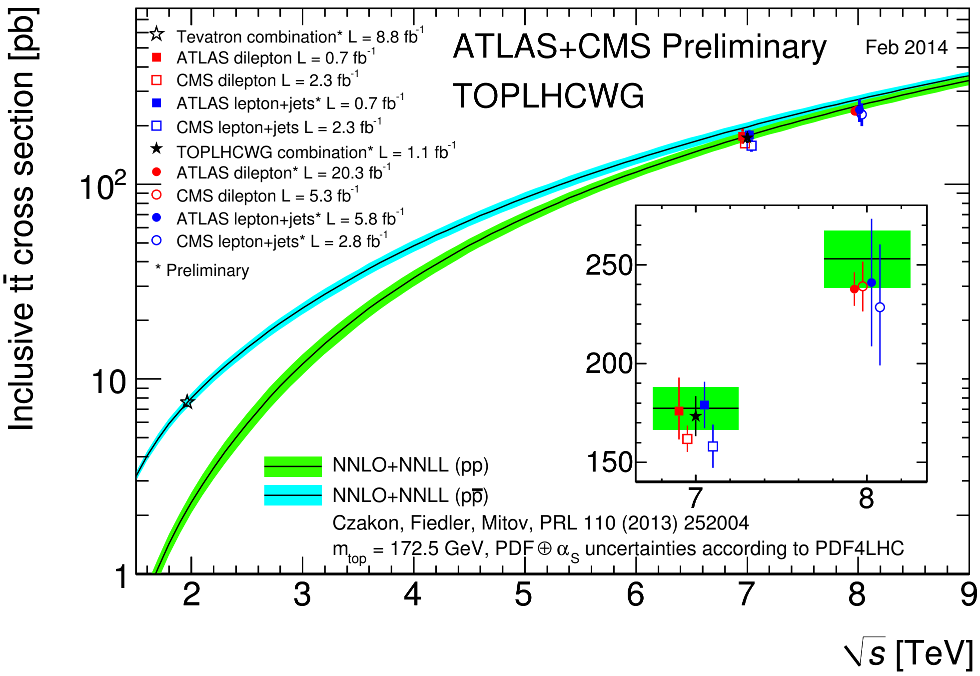

Figure 3.7: A summary of the most precise $t\bar{t}$ production cross section measurements performed at the LHC at $\sqrt{s} = 7$ and 8 TeV and the Tevatron at $\sqrt{s} = 1.96$ TeV compared to the theoretical prediction. Note that the Tevatron results should be compared against the prediction for $p\bar{p}$ collisions while the LHC against the pp collision predictions.

Mass asymmetry measurement

As mentioned in Section 2.3, the charge (C) and parity (P) symmetries are both violated in weak interactions. The CPT symmetry which includes time reversal (T) is the last remaining symmetry which no interaction appears to violate. Any deviations from this symmetry would have major implications on particles physics [14] and could manifest itself as differences between matter and antimatter particles. As the only quark which can be studied directly, measurement of $\Delta m \equiv m_t - m_{\bar{t}}$ could hint at any such deviation produced by new physics. Such a measurement was conducted by the ATLAS [15] experiment yielding the result:

$$\Delta m_t = -0.44 \pm 0.46 \text{ (stat)} \pm 0.27 \text{ (stat) GeV} \tag{3.1}$$

and by the CMS [16] experiment yielding the result:

$$\Delta m_t = 0.67 \pm 0.61 \text{ (stat)} \pm 0.41 \text{ (stat) GeV} \tag{3.2}$$

which are both consistent with the SM prediction and imply CPT invariance.

Charge asymmetry

Many BSM theories can affect the charge symmetry between top and antitop quarks. Once again any deviations from the SM prediction would point to the existence of new BSM physics. The charge asymmetry as measured by the ATLAS experiment [17] is $A_C = 0.006 \pm 0.010$ and $A_c = -0.010 \pm 0.017 \pm 0.008$ for CMS [18], which once again are consistent with the SM prediction.

Chapter 4

The LHC and the ATLAS Detector

This section will include a description of the Large Hadron Collider and the ATLAS detector technology with particular emphasis on those aspects that allow for precision measurement of muons and top quark physics studies.

4.1 The Large Hadron Collider

4.2 The ATLAS detector

Chapter 5

Identifying b-jet, and the Match χ^2 based Soft Muon Tagger

This section will include a description of several current methodologies for b-jet tagging and a detailed description of the Match-χ^2 Soft Muon Tagger.

5.1 b-jet tagging methodology

5.2 The Match-χ^2 Soft Muon Tagger

Chapter 6

Calibration of the Soft Muon Tagger for 2012 ATLAS Data

High-energy physics relies heavily on the use of simulated data to inform the development of analysis techniques. It is thus paramount that the simulation reflect nature as closely as possible. However the simulation does not accurately predict conditions within the detector and the effects on the muon reconstruction and the quality of the fit between the inner detector tracks and muon spectrometer tracks which is represented in the χ^2_{match}. Instead the difference between simulation and data is quantified and taken into account. This process is known as calibration. In the case of the muon reconstruction method and the χ^2_{match} tagger it is important that the difference in efficiency between MC and data be accounted for. This is done by constructing a scale factor, defined in this case by:

$$\kappa_{\chi^2_{\text{match}}} = \frac{\epsilon^{\text{Data}}_{\chi^2_{\text{match}}}}{\epsilon^{\text{MC}}_{\chi^2_{\text{match}}}} \tag{6.1}$$

One of the advantages of using the χ^2_{match} tagger over other forms of tagging is that the presence of a jet is not required to measure the χ^2_{match} of a muon. This means that the calibration can be performed on a isolated muons such as those from $J/\psi \to \mu\mu$ or $Z \to \mu\mu$ using the so called tag and probe method. This calibration relies on muons with low p_{T} from J/ψ decays. As the χ^2_{match} is a characteristic of combined and therefore reconstructed muons,

The tag and probe method used in this calibration is defined as follows. One reconstructed combined muon is designated as the Tag, this muon must pass a stringent set of cuts implying that this is indeed a muon from a J/ψ. The second muon which is designated as the Probe is constructed from an inner detector (ID) only. To ensure that the Probe is the second muon from the J/ψ decay, the invariant mass of the combined tag and probe system is required to be within a mass window centered around the true J/ψ mass. The complete selection used in the calibration is detailed in Section 6.1. These Probes are then used to measure the reconstruction efficiency and the χ^2_{match} tagger efficiency as described in Sections 6.2 and 6.3.

The tag and probe method used here is based on a previous calibration of the χ^2_{match} tagger performed on 2011 ATLAS collision data outlined in This analysis differs from the 2011 calibration in several ways these will be highlighted and explained.

6.0.1 Software, Collision Data and Simulated samples

The tag and probe method used here was implemented using the ROOT analysis framework.

The calibration was performed on a dataset made of those luminosity blocks selected by the recommended standard Good Runs List (GRL) which corresponds to all *pp* collision periods in 2012. The GRL selects only those luminosity blocks where detector conditions are appropriate for physics data-taking. This includes all relevant detector components being operational and that stable beam conditions have been achieved. The datasets are part of the 2013 summer reprocessing (processing tag p1328) corresponding to data taken in periods A through to L, excluding periods F and J.

The efficiency scale factor is measured against a sample containing almost 10 million $J/\psi \to \mu\mu$ events. At event generation filters are applied so the sample only contains events where both muons have a transverse momentum of at least 4 GeV and they must lie within the pseudo-rapidity range $|\eta| < 2.5$. This selection matches the object selection used by most analyses as recommended by the Muon Combined Performance (MCP) group.

6.1 Tag and Probe Selection

A tag and probe method was chosen to measure the efficiency of muon reconstruction and the χ^2_{match} tagger. The tag and probe method allows for the measurement of the performance of selection criteria or algorithms by exploiting well known decays. By creating a sample of objects, in this case muons, on which to apply the aforementioned selection criteria, it is possible to study these algorithms.

The muon reconstruction algorithm examines various Inner Detector (ID)tracks and Muon Spectrometer (MS) tracks and makes a determination as to whether said track is produced by muon or not. To measure the performance of the muon reconstruction algorithm a sample of ID tracks which originate from the J/ψ decay and are thus very likely to be a real muon is constructed. This is done in the following way:

First, require the presence of a combined `STACO` muon which passes a very stringent selection. This strongly implies that this is a real muon and thus is labelled as the Tag. Additionally a very loose selection is applied to all ID tracks. These are known as candidate Probes. Pairs of tag and probes are then formed by requiring that the combined invariant mass lie within a J/ψ mass window and the pair pass additional pairing cuts. This then implies that the Probe is likely the other muon from the J/ψ decay and as such is a suitable test-bed to measure the performance of the muon resconstruction algorithm. Note that all selection criteria are detailed and explained in Section 6.1.2

After selecting a sample of probes the performance of the algorithm is estimated by measuring the proportion of probe candidates which are selected by the algorithm. In other words the performance is estimated by counting the number of muons which are reconstructed given that the ID track is very likely to be a real muon. Probes which are reconstructed into combined `STACO` muons are labelled as muon probes. The performance of the χ^2_{match} tagger is estimated in a similar manner, by measuring the proportion of combined muon probes which pass the SMT selection.

6.1.1 Trigger requirements

In order for an event to be included in the analysis it must pass at least one of the trigger chains listed in Appendix A. For the sake of brevity only the primary trigger (`EF_mu6_Trk_Jpsi_loose`) which contributes the majority of events is described here.

As stated in the trigger name this is an Event Filter trigger which requires the presence of a muon with a momentum of at least 6 GeV and an ID track whos combined invariant mass lies within a J/ψ mass window of 2.6 GeV $< m_{\text{inv}} <$ 3.6 GeV. This loose mass window contains the entirety of the J/ψ peak in all examined p_T and η ranges as well as additional side bands to allow for background removal. Note the omission of double muon triggers to avoid introducing a bias by specifically selecting events with two good muons.

Also note that while all triggers are operational in all periods, most are heavily prescaled and the prescale is period dependent. This does not have a first-order effect on the measurement since only ratios are compared between collision data and MC.

6.1.2 Selection Cuts

The selection criteria for tags, probes, muon probes and SMT muons are listed and detailed below. Note that all cuts are applied on the kinematic properties measured in the ID due to its improved resolution unless it is not possible as in the case of the χ^2_{DoF} which is a combined MS and ID property. Also note that all objects must pass a selection criteria collectively refered to as MCP cuts. These are tracking quality cuts which require a certain number of detector elements be active to ensure good tracking. These cuts are listed in

The muon tag selection criteria are defined in the list below:

- MCP cuts
- `STACO` collection
- Combined muon
- p_T >4 GeV
- $|\eta|$ <2.5

- $|d_0|$ <0.3 mm and $|z_0|$ <1.5 mm
- $|d_0/\sigma_{d_0}|$ <3 and $|z_0/\sigma_{z_0}|$ <3
- Fired at least one of the relevant triggers (see Appendix A)

Included are cuts on the muon impact parameter (IP) d_0 and z_0. These are defined as the distance of closest approach of the ID track to the primary interaction vertex in the transverse and longitudinal planes, respectively. Additionally cuts on the absolute values of IP significances are also implemented. The signifiance of the impact parameter is defined as d_0/σ_{d_0} where σIP is the standard deviation of the impact parameter. These cuts are designed to ensure that the muon selected originates near the primary vertex and thus from a prompt J/ψ from the primary collision. Note that non-prompt J/ψ can be produced in the decay of b hadrons. Finally note that the tag muon must match the trigger object which selected this event.

The probe selection is a subset of the tag selection and only requires an ID track with $|\eta| < 2.5$ and $p_T < 4$ GeV. The pairing cuts are shown below:

- 2 GeV $\leq m_{\text{inv}} \leq$ 4 GeV
- Probe charge is opposite the tag charge
- 0.4 < ΔR(tag, probe)< 3.5
- Δz_0(tag, probe)< 0.2 mm

The probe and the tag are required to be fairly well separated to avoid the momentum of the tag from entering the isolation cone of the probe. In the 2011 calibration analysis the track of the tag and the probe are refit to a common vertex and the quality of the refit, expressed by the χ^2 is a part of the pairing criteria. This criteria is present to reduce the effects of pile-up on the measurement, by ensuring both objects have a common origin. Since the data format used for this analysis is a derived form of that used in 2011 it is not possible to perform such a refit. Instead the difference between the z_0 of the tag and the probe is used.

The `STACO` reconstruction efficiency is not measured by applying the algorithm on the probe collection but rather a probe is said to be a muon probe if it matches a combined muon from the `STACO` collection. This is done by requiring the angular separation between the probe and the `STACO` muon be less than 0.001. Probes which are matched become the numerator of the reconstruction efficiency and the denominator is defined as the number of probes:

$$\epsilon = \frac{N_{\text{muon probe}}}{N_{\text{probe}}}$$

A muon probe is said to be an SMT muon if it passes the following selection, which matches the muon cuts defined in Chapter 5. Note in particular the main component of the soft muon tagger, the cut on $\chi^2_{\text{match}}/N_{\text{dof}} < 3.2$, the distribution of the χ^2_{DoF} is shown in Fig. 6.1

- $|d_0| < 3$ mm
- $|z_0 \sin(\theta)| < 3$
- $\chi^2_{\text{match}}/N_{\text{dof}} < 3.2$

Those muon probes which pass the SMT selection are the numerator of the SMT efficiency and the denominator is defined as the number of muon probes:

$$\epsilon = \frac{N_{\text{SMT}}}{N_{\text{muon probe}}}$$

6.2 Invariant mass fitting

The pairing criteria are very effective at selecting J/ψ events, however non-J/ψ background events are also pass the selection. These include combinatiorial background where the wrong tag and probe pair is constructed and Drell-Yan which appears as a continuum below the J/ψ peak.

The number of probes is extracted from a fit to the invariant mass of the dimuon system using a composite function to accomodate for the background and the gaussian-like J/ψ peak.

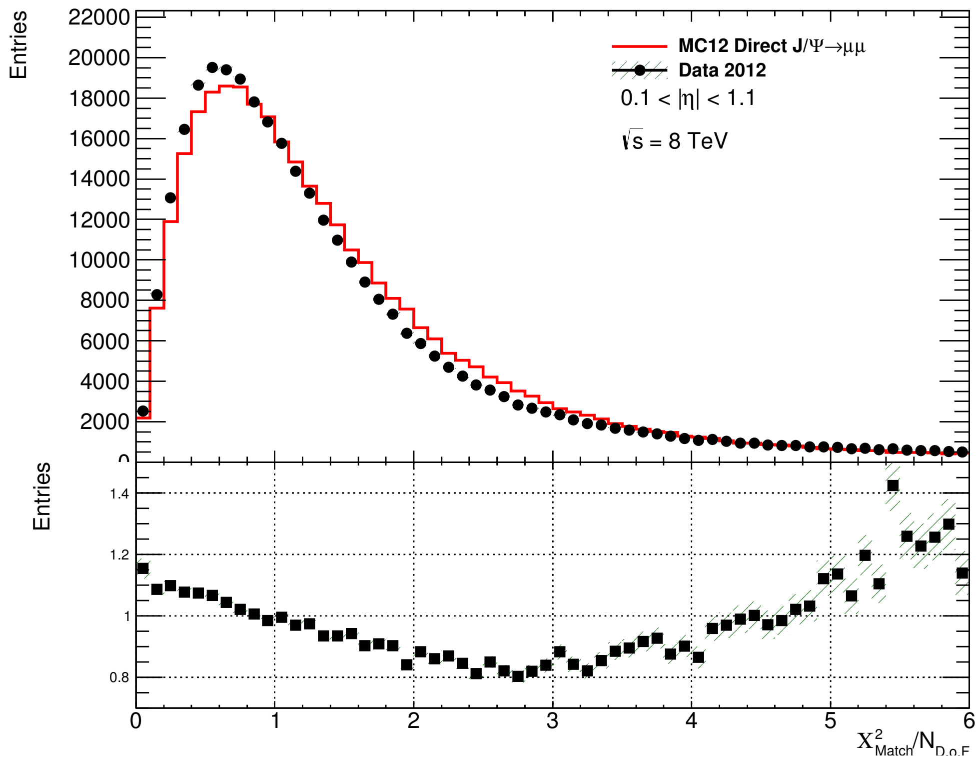

Figure 6.1: The distribution of $\chi^2_{\mathrm{match}}/N_{\mathrm{dof}}$ for all muon probes for ATLAS collision data and prompt J/ψ Monte Carlo simulation.

The invariant mass peak of the J/ψ is modelled by a gaussian distribution while the background distribution is modelled by a quadratic. The invariant mass distribution is fit by a sum of the two functions.

To avoid the first-order effects of signal mis-modelling from the fit of the J/ψ peak, the yield is obtained from the integral of the measured invariant mass distribution subtracting the background contribution from the integral of the fit to the background. The integration is performed in a window with a width based on the width of the fitted J/ψ peak. The integration window marked in Fig. 6.2 corresponds to three times the width of the peak or simply 3σ. Additionally note the composite fit line as well as the background-only distribution and the implied signal gaussian peak.

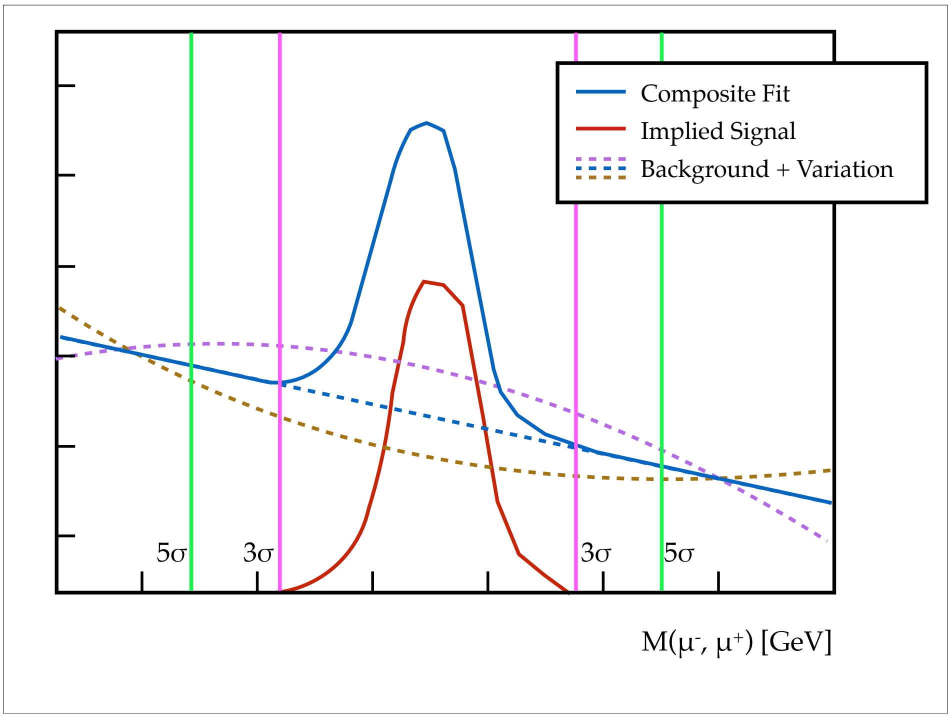

Figure 6.2: A diagram of the various components of the fit procedure. The composite fit is shown along with the corresponding implied signal and background. The two variations of the background shape are also shown.

6.2.1 Uncertainty Measurement

The uncertainty on the efficiency is made of three components. First, the statistical uncertainty on the efficiency is estimated as a Binomial error:

$$\delta\epsilon = \sqrt{\frac{\epsilon \times (1-\epsilon)}{N}} \tag{6.2}$$

Where ϵ is the measured efficiency and N is, in this case the denominator of the efficiency measured.

Secondly, an uncertainty is associated with the fit to the background. This is done by taking the largest upward and downward fluctuations of the background by the uncertainty on the fit parameters of the background, and obtaining the maximum upward and downward effects on the efficiency. After the fit of the composite function is carried out, a downward variation of the background is defined as:

$$f(x) = a_{\text{min}}x^2 + b_{\text{max}}x + c_{\text{min}}, \text{ where } p_{\text{max/min}} = p_{\text{central}} \pm \sigma_p \tag{6.3}$$

Here the maximum and minimum of a parameter is obtained by varying the central value by the uncertainty obtained from the fit. The upward variation of the background fit is thus the opposite, defined as:

$$f(x) = a_{\text{max}}x^2 + b_{\text{min}}x + c_{\text{max}} \tag{6.4}$$

These background variation then result in the maximum deviation from the nominal integral. Again Fig. 6.2 shows these two variations[1]. The uncertainty on the efficiency is then determined by obtaining the maximum efficiency in both directions. If the nominal efficiency is defined as:

$$\epsilon_{\text{nominal}} = \frac{N_{numerator}}{N_{denominator}} \tag{6.5}$$

Then the variations are defined as follows:

$$\epsilon_{\text{up}} = \frac{N^{down}_{numerator}}{N^{nominal}_{denominator}}, \; \epsilon_{\text{down}} = \frac{N^{nominal}_{numerator}}{N^{up}_{denominator}} \tag{6.6}$$

Finally the uncertainty on the background is given by adding the differences between ϵup and ϵdown and the nominal efficiency, in quadrature:

[1]The variation shown in the diagram is very exagerated and meant for illustration purposes

$$\sigma_{\mathrm{bkg}} = \sqrt{|\epsilon_{\mathrm{up}} - \epsilon|^2 + |\epsilon_{\mathrm{down}} - \epsilon|^2} \tag{6.7}$$

The final component of the uncertainty is constructed by varying the integration window. The nominal value is defined as 3σ away from the center of the fitted gaussian, where again σ is the FWHM of the same fitted gaussian. An uncertainty is constructed by measuring the efficiency with a wide integration window corresponding to 5σ. The integration window uncertainty is defined as:

$$\sigma_{\mathrm{window}} = |\epsilon_{5\sigma} - \epsilon_{3\sigma}| \tag{6.8}$$

Finally, the total uncertainty on the efficiency is given by the sum in quadrature of the all uncertainty components. The uncertainty on the efficiency is then carried over to the scale factor determination.

An example of the fitting procedure applied is shown in Fig. 6.3 for both tag and probes at probe level and at muon probe level. Note that as expected the muon probe contains far less background.

6.3 Efficiencies

The efficiency is monitored as a function of a variety of kinematic variables, including isolation variables, transverse momentum and angular position of the probe.

6.3.1 Isolation dependence

The muons from J/ψ used in this calibration are produced in isolation, there is very little energetic activity surrounding them in the detector. In contrast muons from semileptonic decay of b-quarks in $t\bar{t}$ events are produced amongst the numerous components of the b-jets. Thus it is important to ensure that the performance of the χ^2_{match} tagger is not affected by the isolation of the muon for a calibration on J/ψ events to be applicable. In this calibration as, in the 2011 analysis nine isolation variables are considered. The so-called etcone20, 30 and 40 correspond to the transverse energy surrounding the muon in a cone of size $\Delta R = 0.2, 0.3, 0.4$ respectively. Additionally ptcone20, 30 and 40

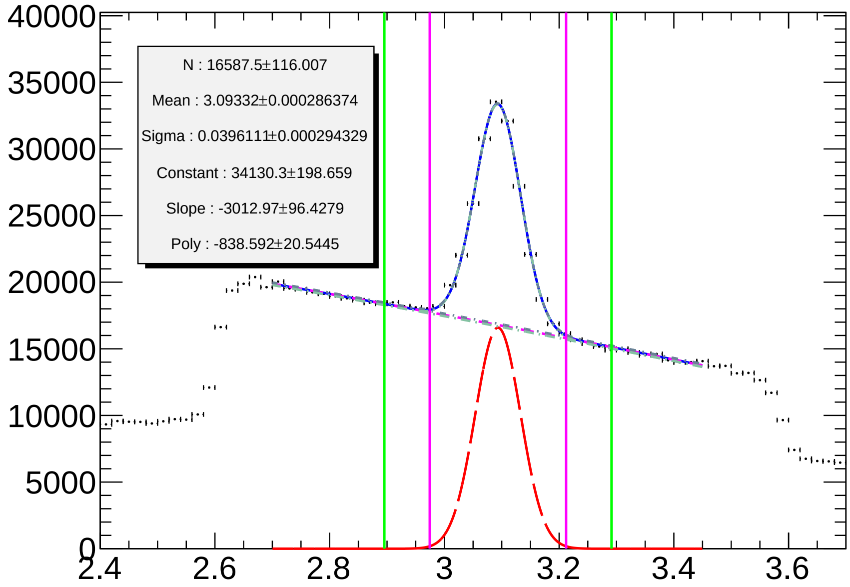

(a) Probe level

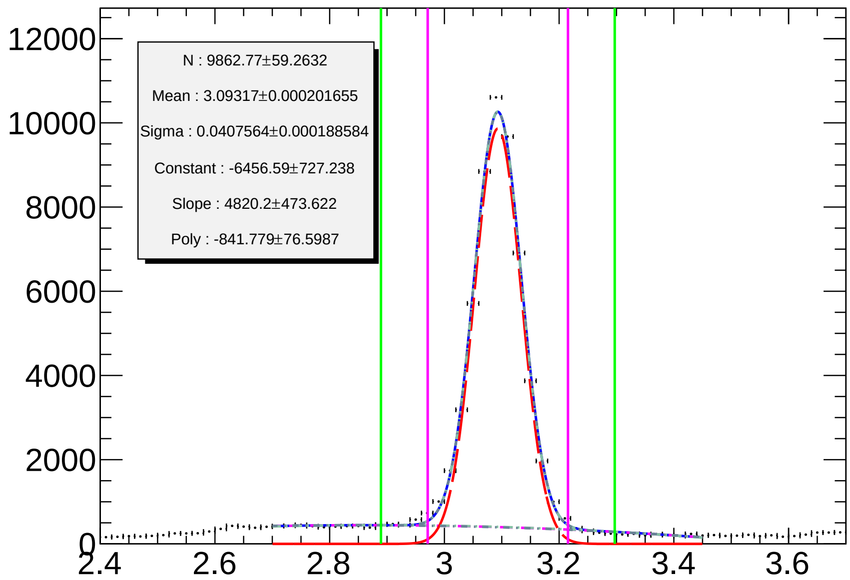

(b) Muon probe level

Figure 6.3: Invariant mass distributions of tag and probe pairs at a) probe level and at b) muon probe level in collision data. Note the various components of the fit as well as the variations on the background fits and the 3σ and 5σ integration windows used for systematics. Note the fit parameters and their respective uncertainties

and nucone20, 30, 40 correspond to the sum of transverse momentum and the number of tracks surrounding the muon, respectively. All nine isolation variables exclude the muon itself in a cone of size 0.1 and include various corrections for known energy losses, momentum leakages between adjacent clusters in the detector and the effects of pile-up.

As in the 2011 analysis there appears to be no dependence of the scale factor on any of the isolation variables examined as can be seen from Figures 6.4, 6.5 and 6.6.

The dependence on each isolation variable is measured in a range dictated by the available statistics. Given the isolated nature of muons in J/ψ events limits the number of muons available at higher pt/et/nucone values.

6.3.2 2011 Calibration

6.3.3 Efficiency Binning

The efficiencies are measured with respect to pseudorapidity and across the $|\eta|$ range of the ATLAS detector in regions defined in Table 6.1. Note that the η regions are label as A and C to denote the positive and negative η sections of the detector. The binning in other variables is determined by the amount of statistics available to allow for the fitting procedure to produce good and stable results. The binning in p_T was chosen as: 4-5, 5-6, 6-7, 7-8, 8-10, 10-12, 12-14, 14-16 and 16-20 GeV.

Table 6.1: Pseudorapidity regions of the ATLAS detector

$\|\eta\|$ range	Name
$0.0 < \|\eta\| < 0.1$	Crack
$0.1 < \|\eta\| < 1.1$	Barrel
$1.1 < \|\eta\| < 1.3$	Transition
$1.3 < \|\eta\| < 2.0$	Endcap
$2.0 < \|\eta\| < 2.5$	Forward

6.3.4 Results

The efficiency is presented as a function of η, ϕ and p_{T}. Figure 6.7 shows the χ^2_{match} efficiency with respect to the spatial variables of the probe. Note that as with the 2011 analysis the efficiency exhibits no dependence on ϕ and an asymmetric dependence on η particularly in the Forward regions of the detector. Note that as expected there is a

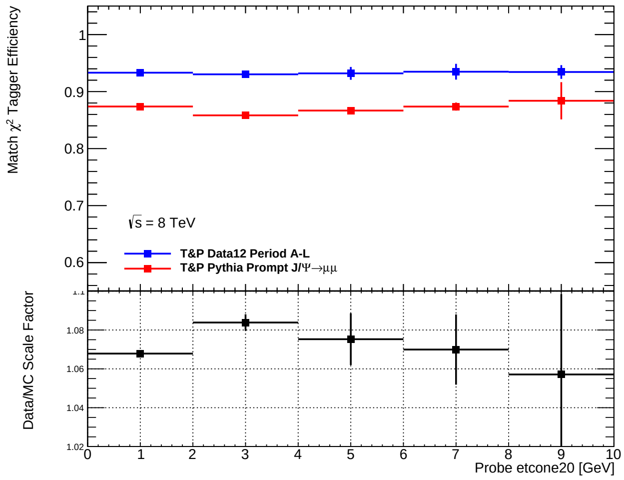

(a) $\sum E_T$ in cone $\Delta R = 0.2$

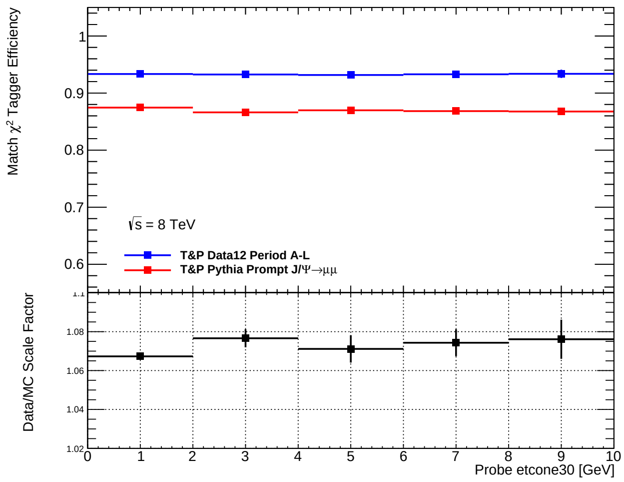

(b) $\sum E_T$ in cone $\Delta R = 0.3$

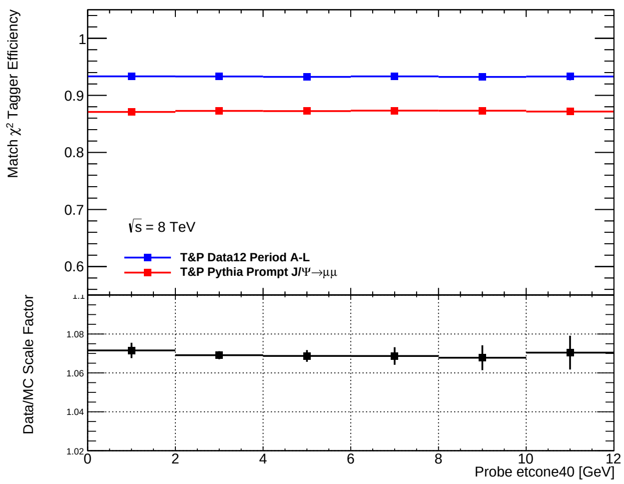

(c) $\sum E_T$ in cone $\Delta R = 0.4$

Figure 6.4: χ^2_{DoF} efficiencies and scale factor with respect to $\sum E_T$.

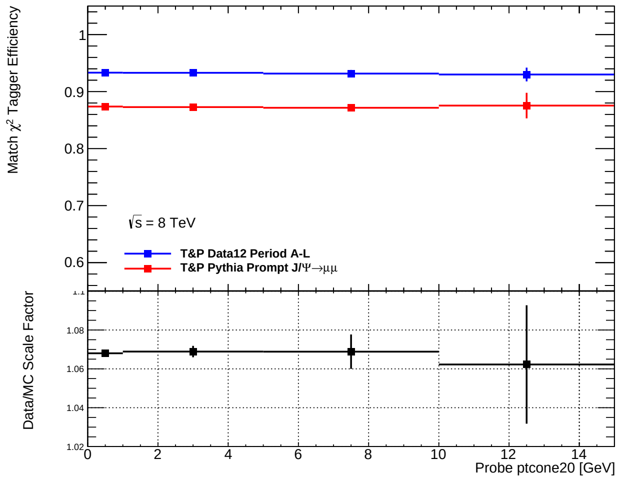

(a) $\sum p_T$ in cone $\Delta R = 0.2$

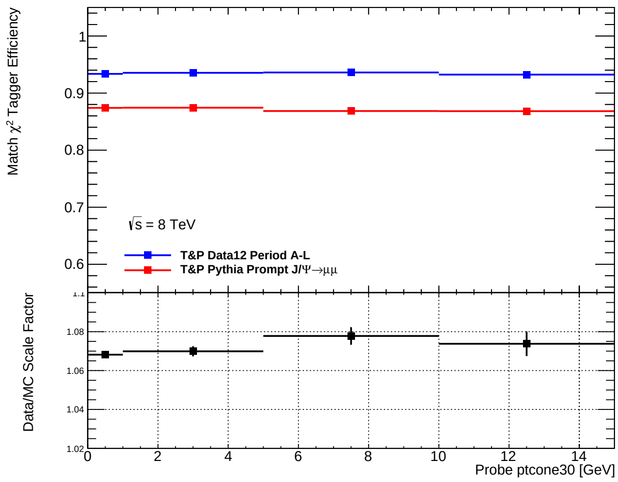

(b) $\sum p_T$ in cone $\Delta R = 0.3$

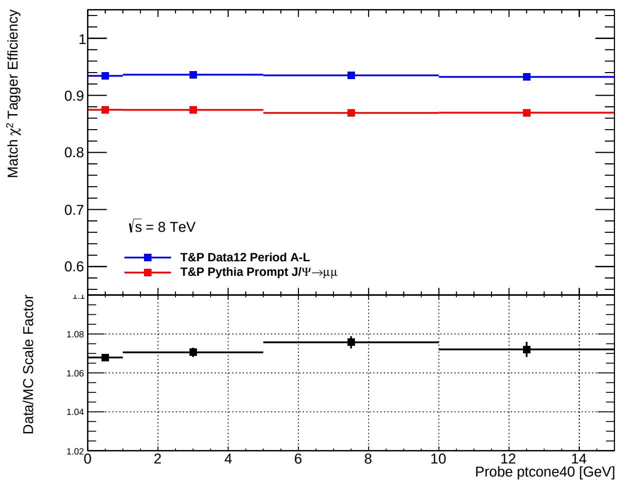

(c) $\sum p_T$ in cone $\Delta R = 0.4$

Figure 6.5: χ^2_{DoF} efficiencies and scale factor with respect to $\sum p_T$.

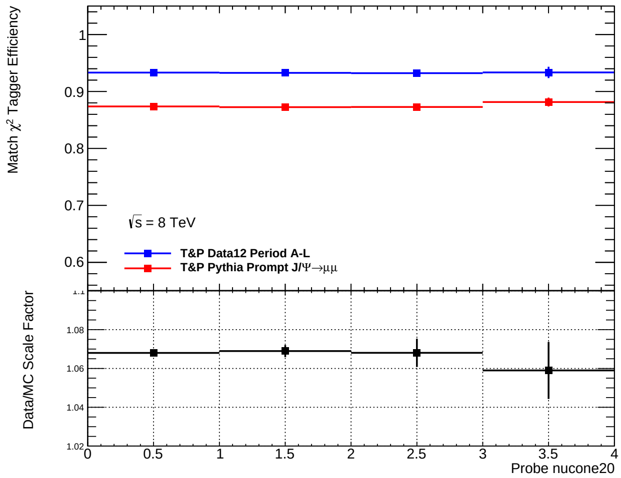

(a) N_{trk} in cone $\Delta R = 0.2$

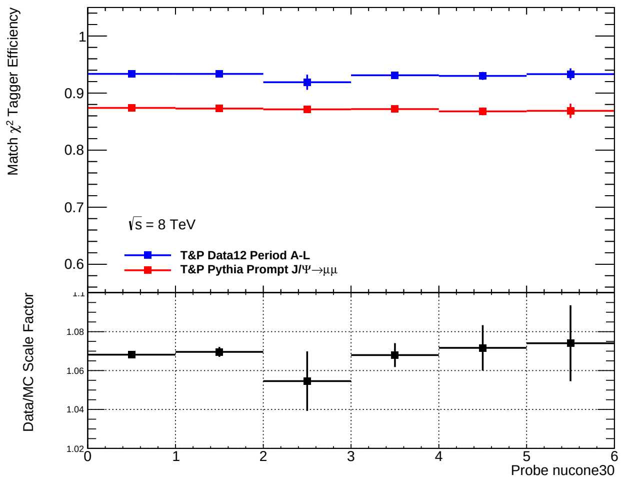

(b) N_{trk} in cone $\Delta R = 0.3$

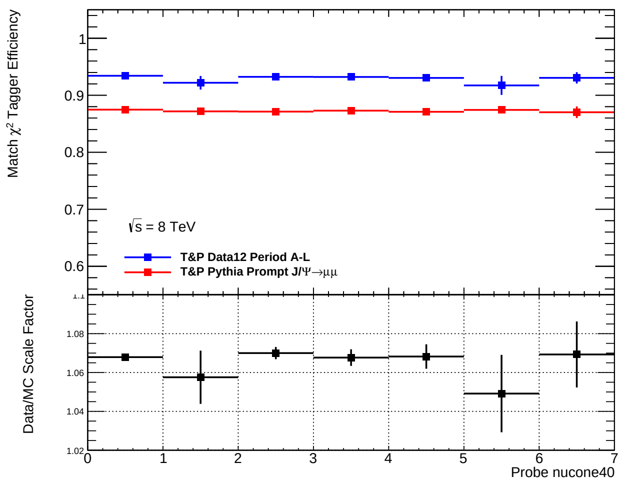

(c) N_{trk} in cone $\Delta R = 0.4$

Figure 6.6: χ^2_{DoF} efficiencies and scale factor with respect various isolation variables.

strong dependence on the transverse momentum of the muon probe as shown in Fig.6.8. As in the 2011 analysis it was decided to bin the scale factor as a function of η and p_{T}. The scale factors and efficiencies are presented in the next pages. The scale factors and their uncertainties are summarized in Table

Table 6.2: Data/MC Scale Factors for 2012 Data in all five regions of the detector as a function of p_{T}. The uncertainties include systematic and statistical components as described in Section 6.2.1

Side A (Positive η)					
p_T range	Crack A	Barrel A	Transition A	Endcap A	Forward A
4-5 GeV	1.051 ± 0.016	1.053 ± 0.005	1.046 ± 0.019	1.061 ± 0.011	1.090 ± 0.018
5-6 GeV	1.050 ± 0.007	1.058 ± 0.004	1.057 ± 0.019	1.062 ± 0.011	1.103 ± 0.020
6-7 GeV	1.068 ± 0.008	1.065 ± 0.003	1.070 ± 0.015	1.065 ± 0.008	1.134 ± 0.019
7-8 GeV	1.061 ± 0.018	1.063 ± 0.006	1.064 ± 0.017	1.061 ± 0.010	1.140 ± 0.024
8-10 GeV	1.061 ± 0.014	1.063 ± 0.007	1.068 ± 0.016	1.052 ± 0.014	1.167 ± 0.023
10-12 GeV	1.060 ± 0.042	1.070 ± 0.006	1.064 ± 0.026	1.058 ± 0.016	1.175 ± 0.038
12-14 GeV	1.061 ± 0.050	1.064 ± 0.010	1.067 ± 0.037	1.057 ± 0.021	1.190 ± 0.057
14-16 GeV	1.062 ± 0.087	1.068 ± 0.015	1.078 ± 0.054	1.067 ± 0.031	1.218 ± 0.064
16-20 GeV	1.062 ± 0.087	1.068 ± 0.015	1.078 ± 0.054	1.067 ± 0.031	1.218 ± 0.064

(a) For the positive η regions

Side C (Negative η)					
p_T range	Crack	Barrel	Transition	Endcap	Forward
4-5 GeV	1.044 ± 0.016	1.055 ± 0.005	1.054 ± 0.017	1.056 ± 0.009	1.068 ± 0.018
5-6 GeV	1.069 ± 0.013	1.057 ± 0.004	1.050 ± 0.016	1.062 ± 0.010	1.084 ± 0.020
6-7 GeV	1.080 ± 0.016	1.068 ± 0.004	1.065 ± 0.008	1.066 ± 0.008	1.089 ± 0.018
7-8 GeV	1.064 ± 0.021	1.068 ± 0.004	1.063 ± 0.016	1.066 ± 0.010	1.095 ± 0.022
8-10 GeV	1.071 ± 0.015	1.067 ± 0.005	1.045 ± 0.015	1.061 ± 0.009	1.107 ± 0.022
10-12 GeV	1.084 ± 0.030	1.073 ± 0.007	1.085 ± 0.022	1.061 ± 0.015	1.113 ± 0.036
12-14 GeV	1.098 ± 0.067	1.069 ± 0.010	1.059 ± 0.031	1.040 ± 0.024	1.108 ± 0.055
14-16 GeV	1.063 ± 0.101	1.073 ± 0.015	1.076 ± 0.046	1.061 ± 0.030	1.099 ± 0.057
16-20 GeV	1.073 ± 0.149	1.088 ± 0.006	1.099 ± 0.028	1.054 ± 0.012	1.117 ± 0.043

(b) For the negative η region

Dependence on d_0

The dependence on the impact parameter d_0 was examined and no direct dependence is observed. From Fig. 6.14 the scale factor shows no structure with respect to d_0 when binned in p_{T}. Since the scale factors are already binned in η and p_{T} the correlation of d_0 and p_{T} is already taken into account.

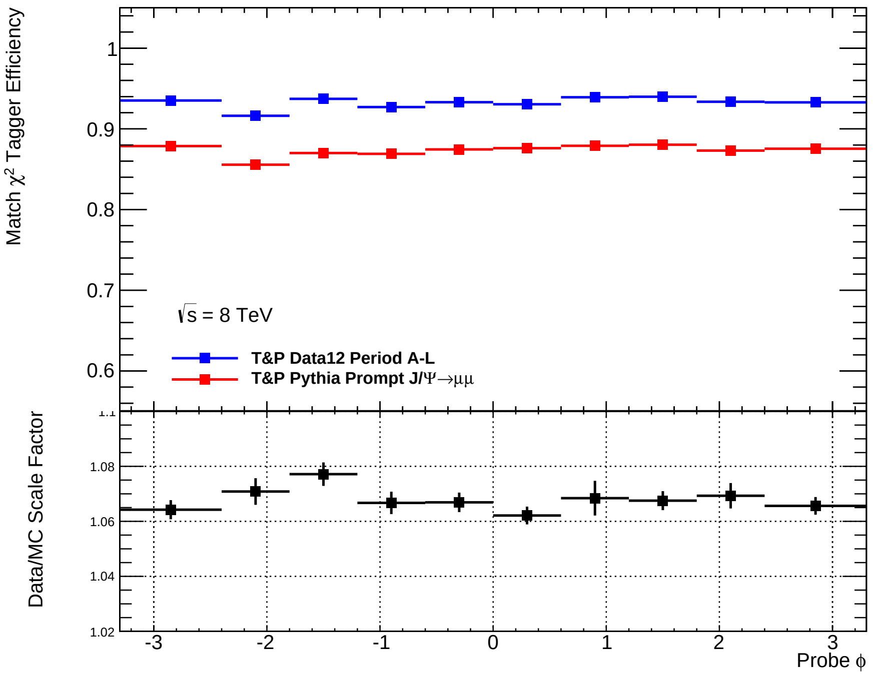

(a) χ^2_{match} efficiency and scale factor as a function ϕ of the probe muon

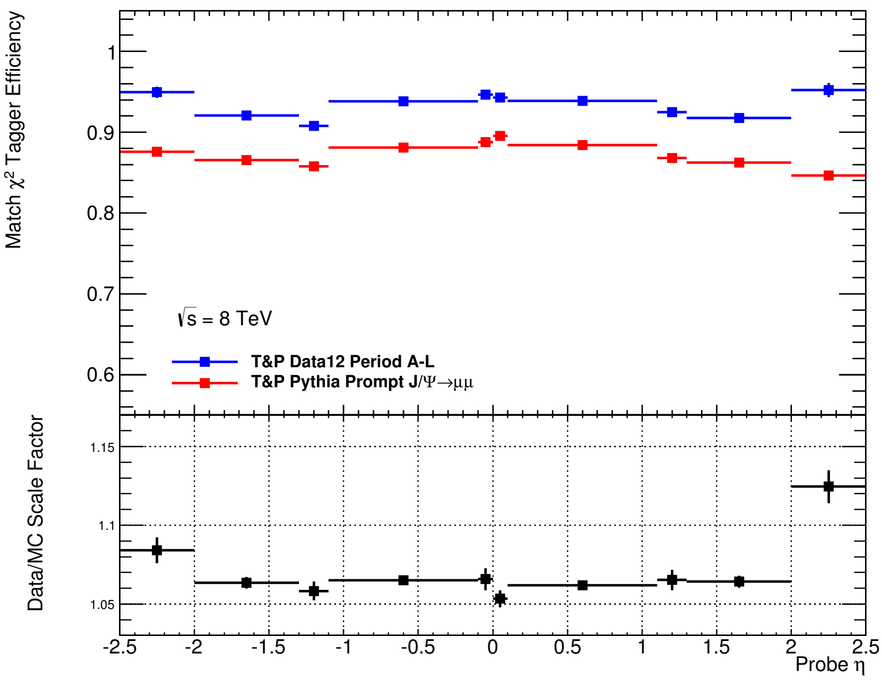

(b) χ^2_{match} efficiency and scale factor as a function η of the probe muon

Figure 6.7: χ^2_{match} efficiencies and scale factor with respect to the (a) ϕ and (b) η

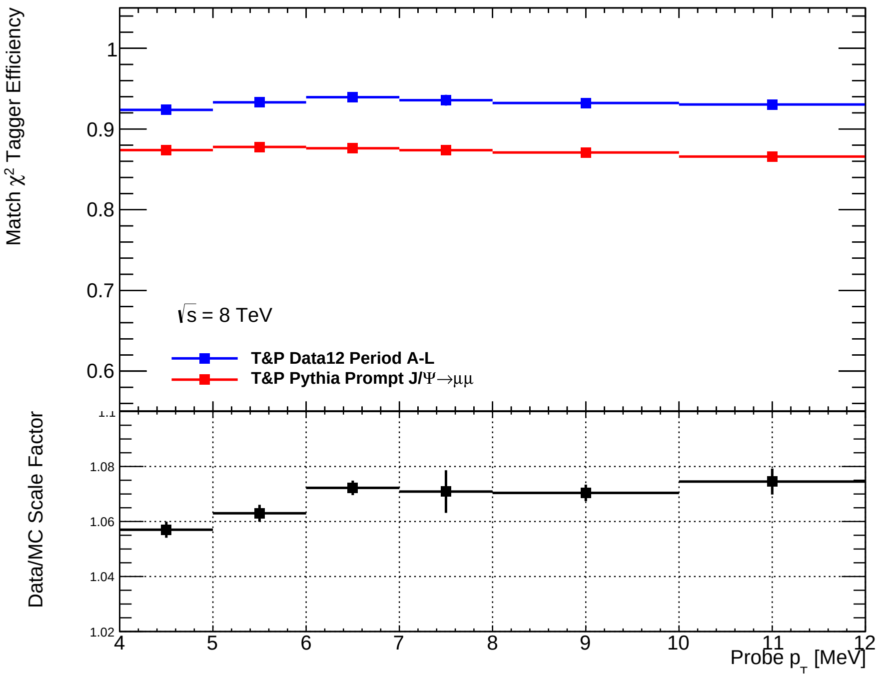

Figure 6.8: χ^2_{match} efficiencies and scale factor with respect to the transverse momentum of the muon probe

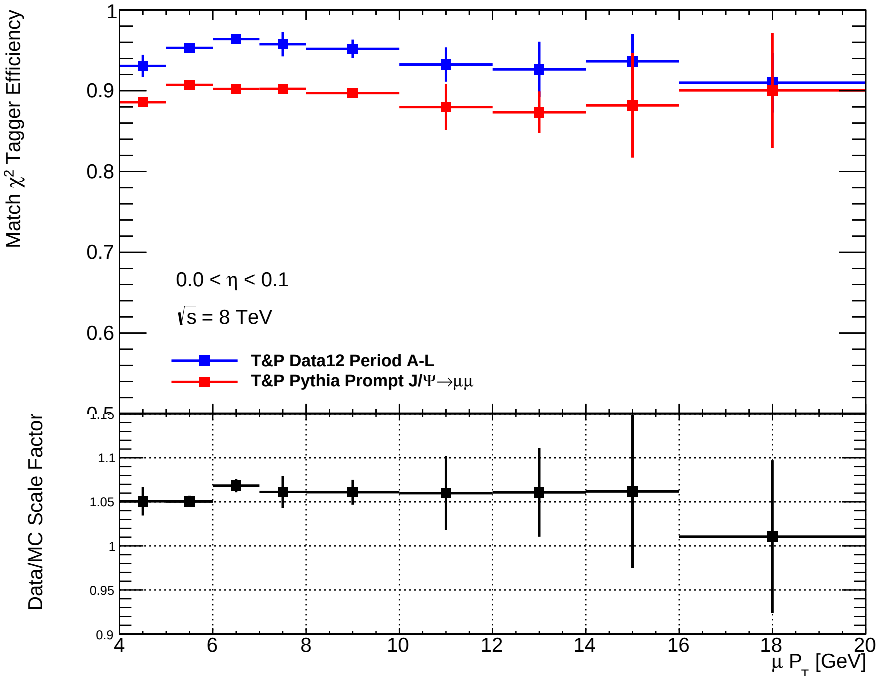

(a) Crack A Region

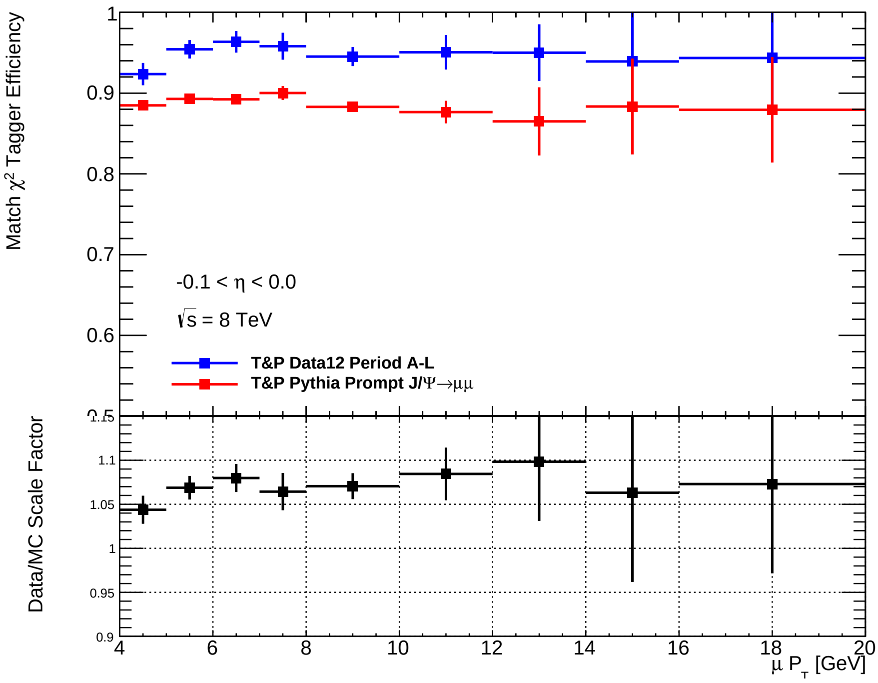

(b) Crack C Region

Figure 6.9: χ^2_{match} efficiencies and scale factors in the crack region of the detector for side (a) A and (b) C

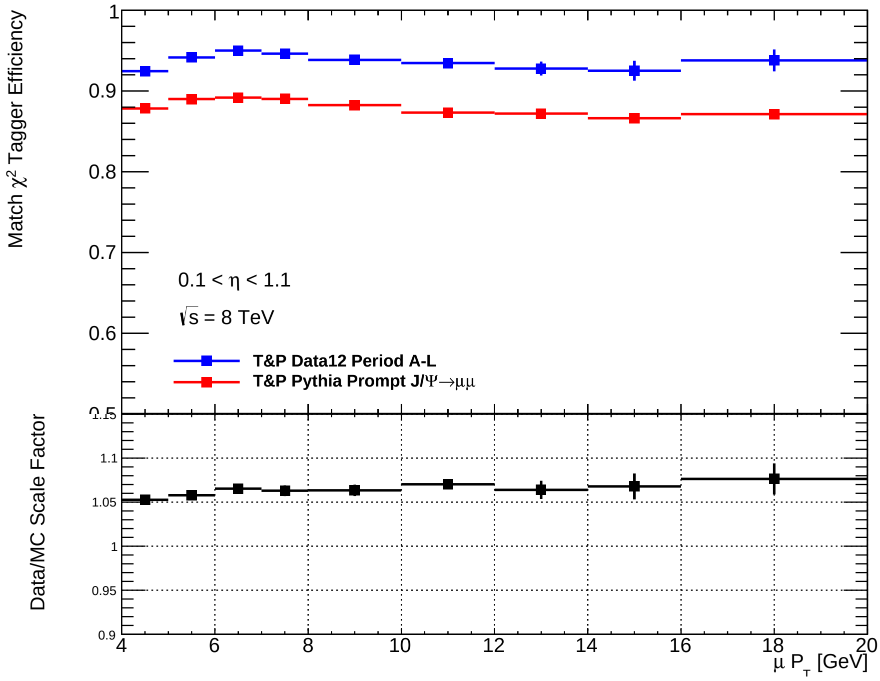

(a) Barrel A Region

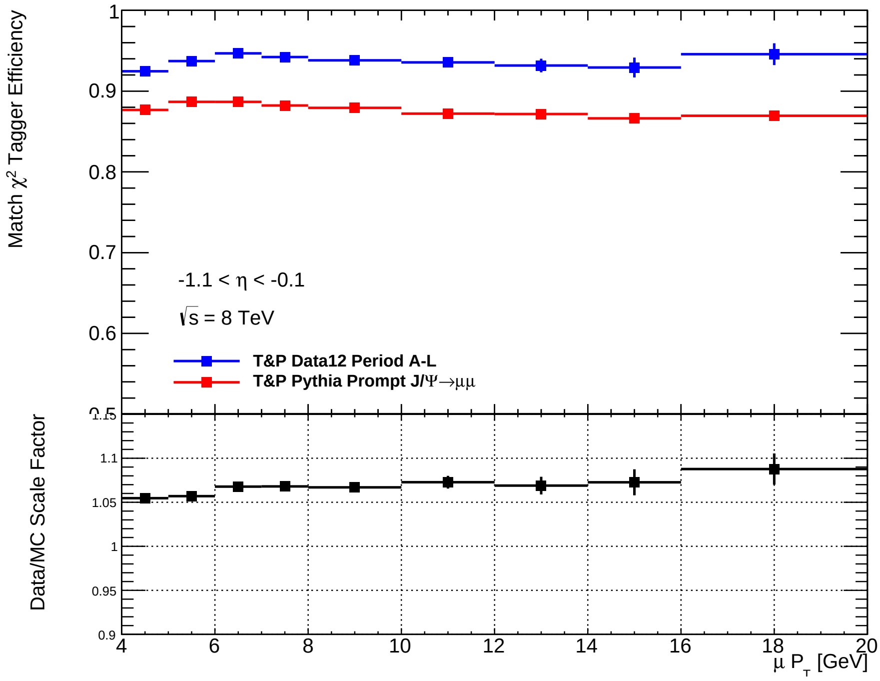

(b) Barrel C Region

Figure 6.10: χ^2_{match} efficiencies and scale factors in the barrel region of the detector for side (a) A and (b) C

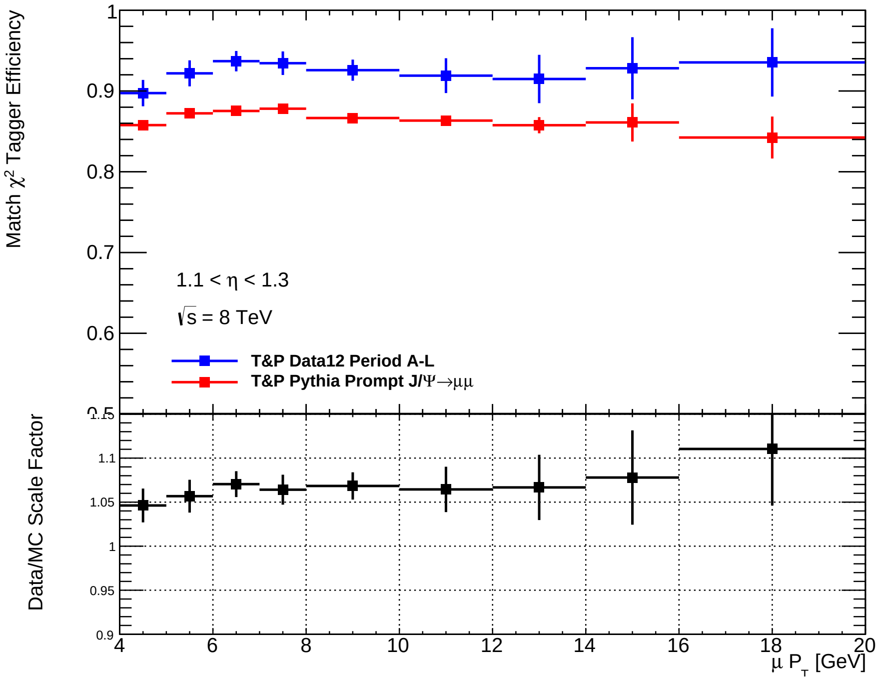

(a) Transition A Region

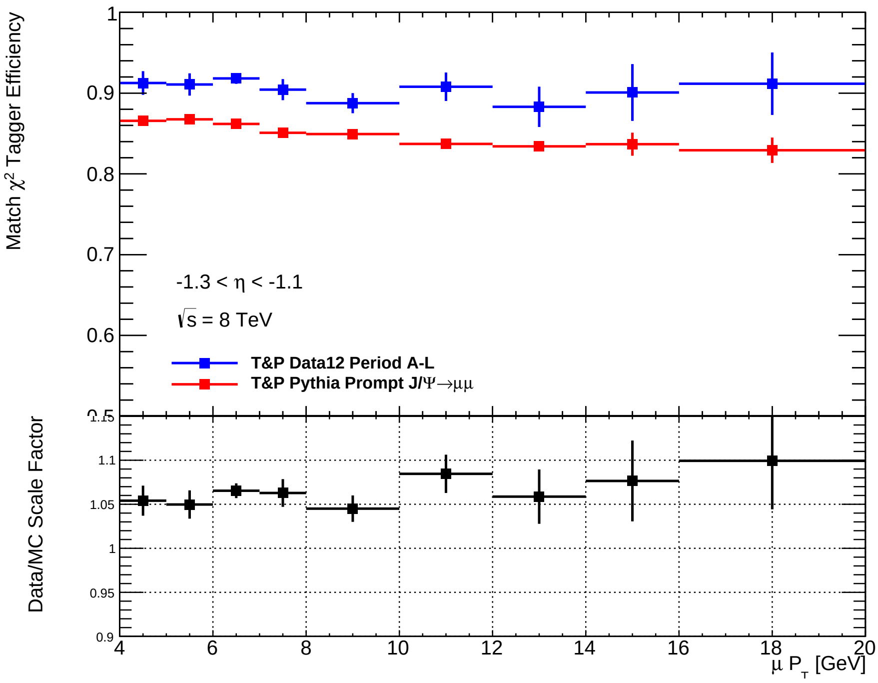

(b) Transition C Region

Figure 6.11: χ^2_{match} efficiencies and scale factors in the transition region of the detector for side (a) A and (b) C

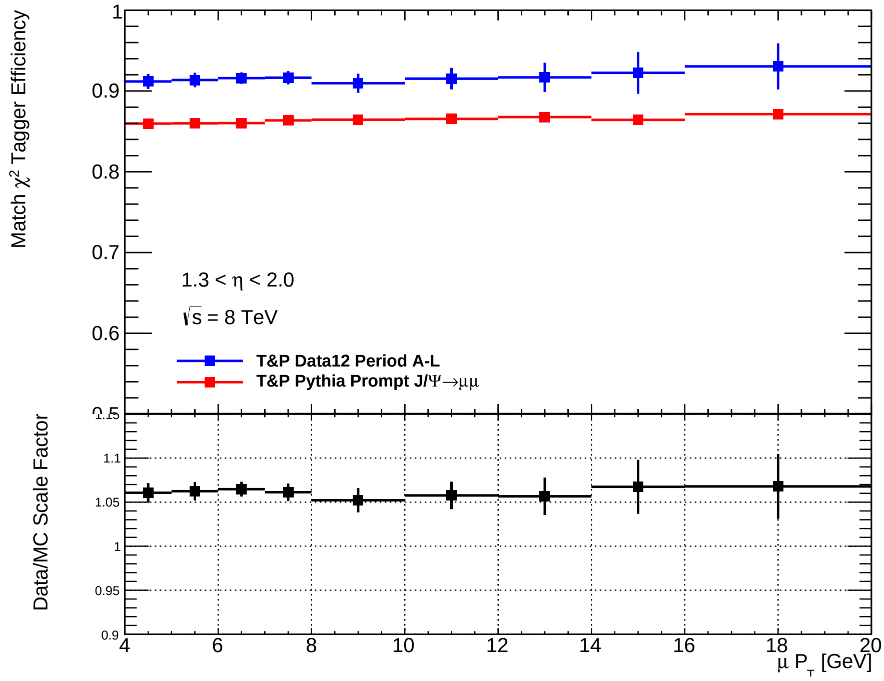

(a) Endcap A Region

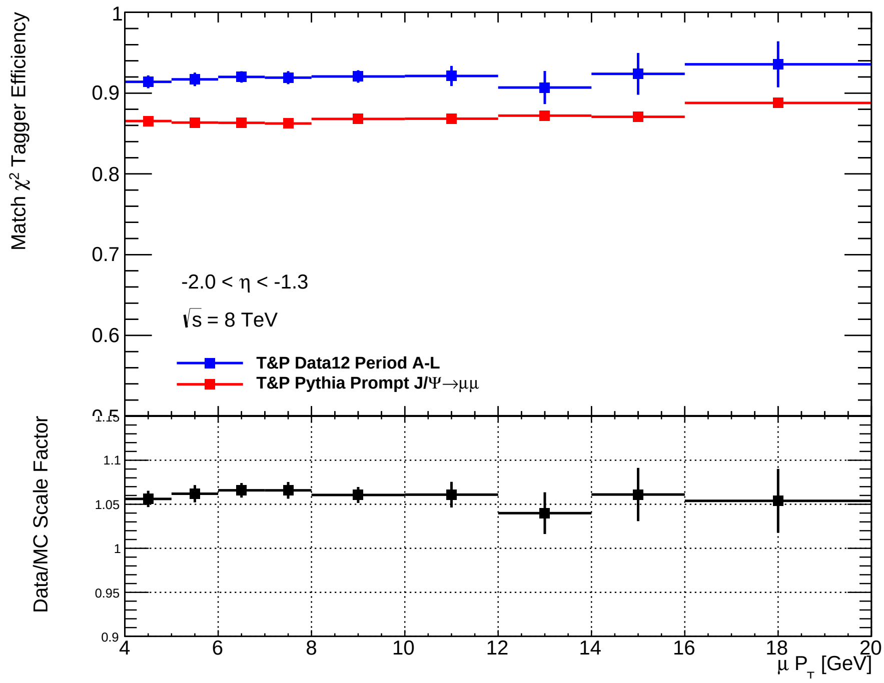

(b) Endcap C Region

Figure 6.12: χ^2_{match} efficiencies and scale factors in the endcap region of the detector for side (a) A and (b) C

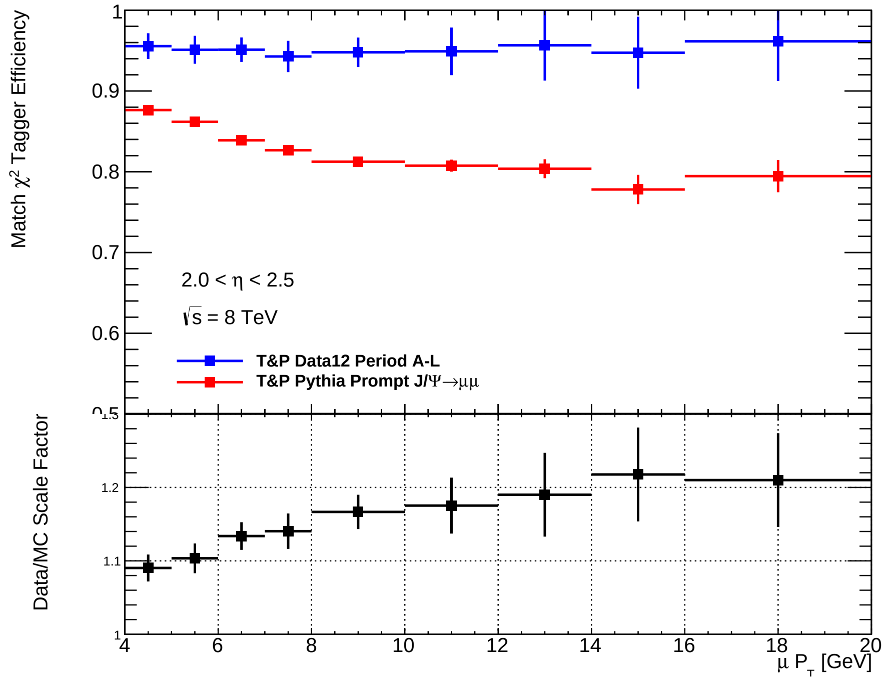

(a) Forward A Region

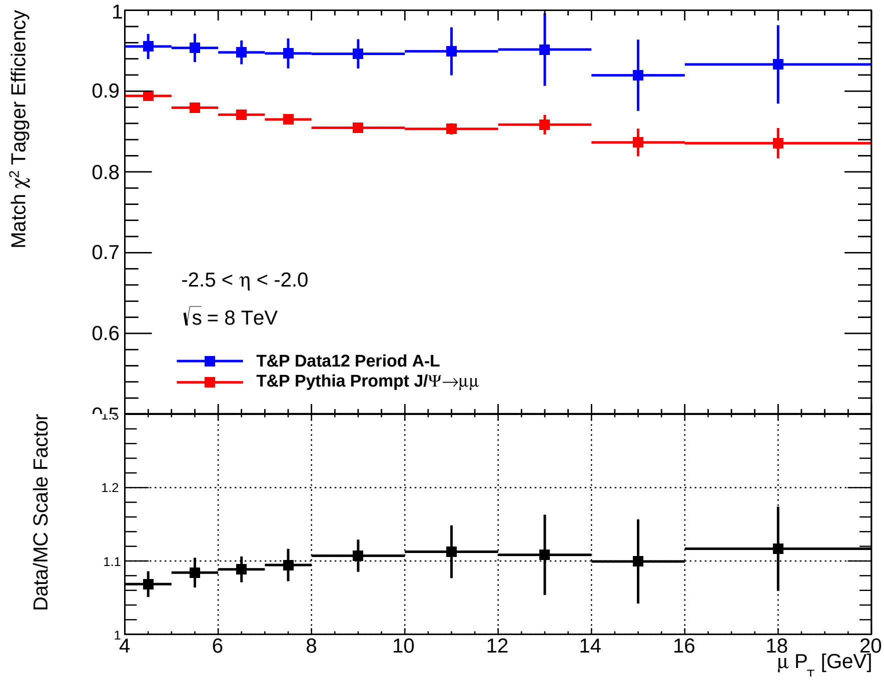

(b) Forward C Region

Figure 6.13: χ^2_{match} efficiencies and scale factors in the forward region of the detector for side (a) A and (b) C

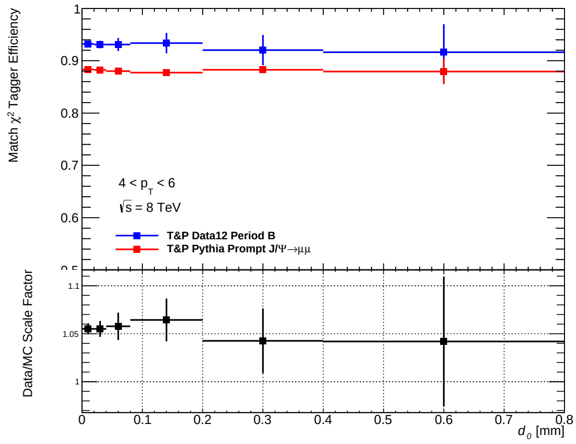

(a) 4 GeV< p_{T} <6 GeV

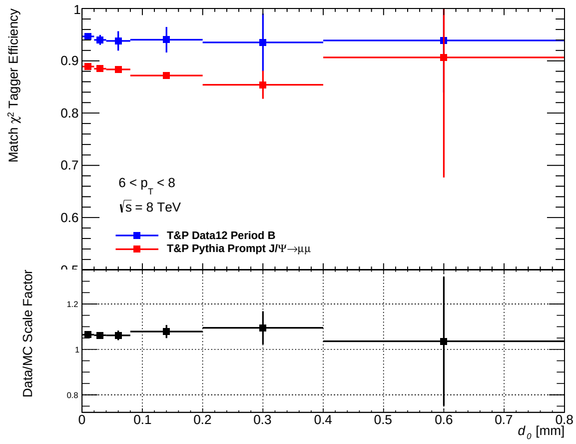

(b) 6 GeV< p_{T} <8 GeV

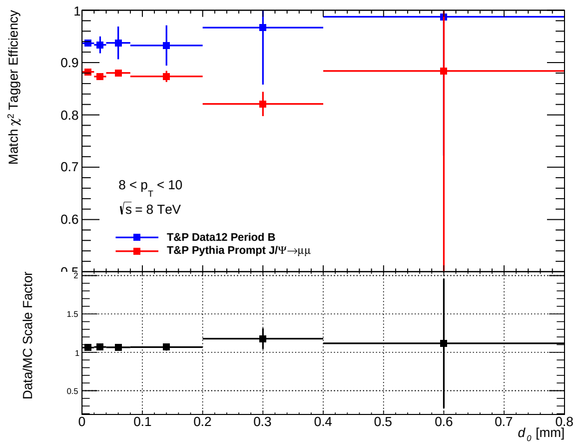

(c) 8 GeV< p_{T} <10 GeV

Figure 6.14: χ^2_{match} efficiencies and scale factor with respect to impact parameter d_0 for muon probes with p_{T} in the range (a) 4-6 GeV, (b) 6-8 GeV and (c) 8-10 GeV. The measurement was carried out only on Period B of 2012 ATLAS collision data.

Chapter 7

Measurement of the $t\bar{t}$ cross-section in the single-lepton channel using SMT

This section will discuss the measurement of the $t\bar{t}$ cross-section in the single-lepton channel with an emphasis on the electron multijet background estimation conducted.

7.1 Data and Monte Carlo samples

This section will

7.2 Object selection and event selection

7.3 Re-weighting of the b-quark to muon transition BR

7.4 Data-driven background selection

7.5 Systematics uncertainties

7.6 Results and conclusion

Chapter 8

Muon Tagging in a boosted $t\bar{t}$ environment

The large center-of-mass energies at which collisions occur at the LHC allows for the production of very high mass particles. Several Beyond the SM (BSM) theories predict the existence of high mass particles which decay primarily top quark pairs. An example of hypothetical model which predict high mass $t\bar{t}$ resonances is the topcolor assisted technicolor model (TC2), which predicts the existence of a leptophobic Z' boson. The resultant top quark pair provides a well understood probe to search for such hypothetical particles.

The Z' could potentially have a mass on the order of several TeV. As a result their decay product would be produced in the detector with very large momentum. These top quarks are said to be boosted. In terms of the subsequent top decay, the resultant bottom quark and W boson are expected to emerge in a collimated cone. The events thus appear as two large back-to-back jets. If the W decays leptonically, the W lepton is expected to lie very close to or within the b-jet. If the W decays hadronically all three jets will appear to merge into a single 'fat' jet.

In this chapter the results of a feasibility study conducted to determine the viability of using the χ^2_{match} tagger to tag W muons from boosted top-quark decays is presented and discussed. Note that this is in contrast to the cross-section analysis detailed in a previous chapter where the muon tagged came from the semileptonic decay of b-quarks.

The boost is expected to be related to the mass of the Z' produced, so a higher mass Z' would decay into more collimated jets. The environment that results is thus very similar to that of a semileptonic b-decay, a muon buried inside of a b-jet.

No evidence for such a resonance has been observed and limits have been placed on the production rate of these resonance for various benchmark models. A leptophobic topcolor Z' of mass less than 1.74 TeV has been excluded using 4.7 fb^{-1} of pp collision data collected by ATLAS with a center-of-mass energy $\sqrt{s} = 7$ TeV [19]. Additionally a more recent analysis using 14.3 fb^{-1} of $\sqrt{s} = 8$ TeV data collected at ATLAS excluded a Z' with a mass less than 1.8 TeV at 95% confidence level [20]. The analysis detailed here is based on the 7 TeV analysis. Similar analyses performed with data collected by CMS have excluded Z' candidates for similar benchmark models [21–23].

The performance of SMT is compared to the contemporary method for selecting muons known as mini-isolation. In addition a short performance study to determine the viability of using SMT to tag b-jets in boosted top events is also presented. Firstly, a short examination of the topology of a boosted event is presented.

8.1 Boosted event topology

In order to perform an effective feasibility study, it is important to understand the signature left by boosted events in the detector. There are certain expectations regarding the momentum distribution of the various product particles from the decay of the top as well as their angular separation. As with the cross-section analysis presented in Chapter 7, this study focuses on the semileptonic decays of top quark pairs

It is expected for events where the momentum of the top quarks higher to exhibit stronger collimation between the W muon and the b-quark. This results in a situation very similar to that exploited for muon tagging in Section 7 where a muon from the semileptonic decay of a b-quark emerges from within the b-jet. Fig. 8.1 illustrates the similarity of both scenarios. It is thus possible to use the χ^2_{match}-tagger[1] to tag W muons in boosted events. As the tagger is designed to work in energetically "busy" sectors of the detector, it is ideally suited to probe highly boosted events where the decay products

[1]As signal muons are very hard, the tagger is now refered to as the χ^2_{match}tagger not soft muon tagger to reflect this difference

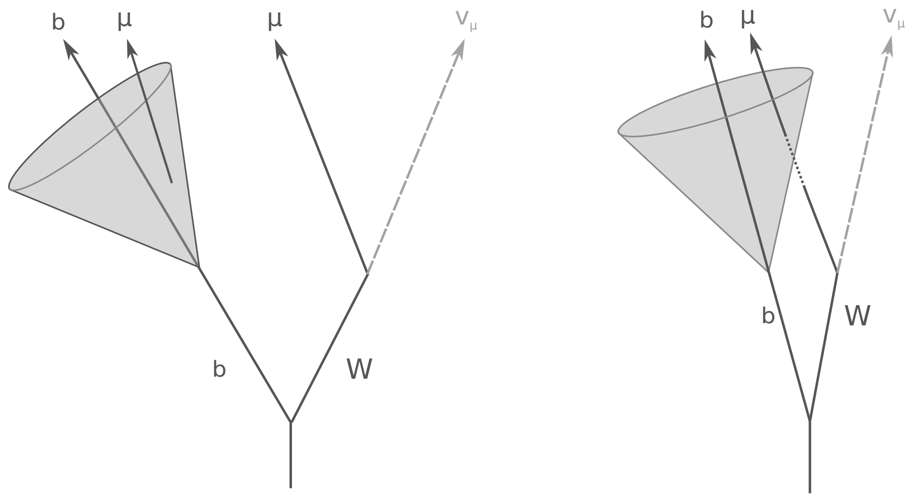

(a) Non-boosted event (b) Boosted event

Figure 8.1: This figure shows a simple diagram for the possible configuration of final-state objects in a (a) boosted and (b) non-boosted events. Note that in both cases a muon is embedded within the b-jet

are collimated.

As can be seen from Fig. 8.2 the increase in boost does result in the W muon and b-quark emerging closer. Note that the fraction of events below the SMT requirement of $\Delta R(\mu, jet) < 0.5$ increases with increased top-quark p_{T}. Additionally Fig. 8.3 shows that the top p_{T} distribution peaks at just below half of the mass of the Z' boson, thus the large portion of the candidate muons in the sample will pass the aforementioned separation requirement. The decay products of the top quark appear to emerge primarily back to back as seen in Fig. 8.4.

8.2 Samples and muon selection

This measurement is based on simulated data generated for a Z' with a mass of 1.0, 1.3, 1.6, 2.0, 2.5 and 3.0 TeV. All Monte Carlo (MC) samples were generated using PYTHIA with CTEQ6LI PDFs. The width of the generated Z' is 3% of the mass.

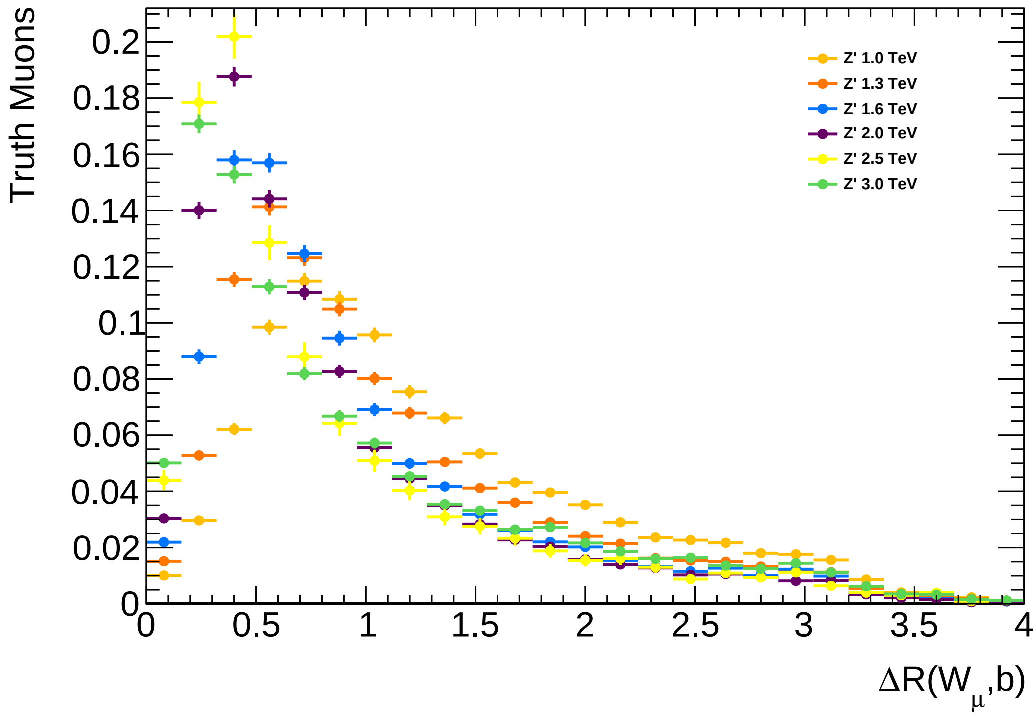

Figure 8.2: The angular separation (ΔR) between the truth W muon and the corresponding b-quark for all examined Z' mass points.

8.3 Signal muon selection

8.3.1 Muon selection

The nominal muon object selection includes an isolation requirement, which normally removes events where the signal lepton is found in a region of the calorimeter with large amounts of activity. Cutting on the amount of energy deposited in the calorimeter around the lepton is an example of one such requirement. Such a cut forms part of the object selection used in the top cross-section measurement described in Part 6.

However, as described a priori, boosted top events result in large collimated jets which include the products of the two top quarks. Thus the signal lepton can emerge within the cone of the reconstructed jet from the b-quark.

Note that the muon is not required to be isolated, instead the muon is tagged by the χ^2_{match} tagger. Selecting isolated muons would reduce significantly the number of muons available for tagging. Additionally, as explained a priori, events which exhibit stronger

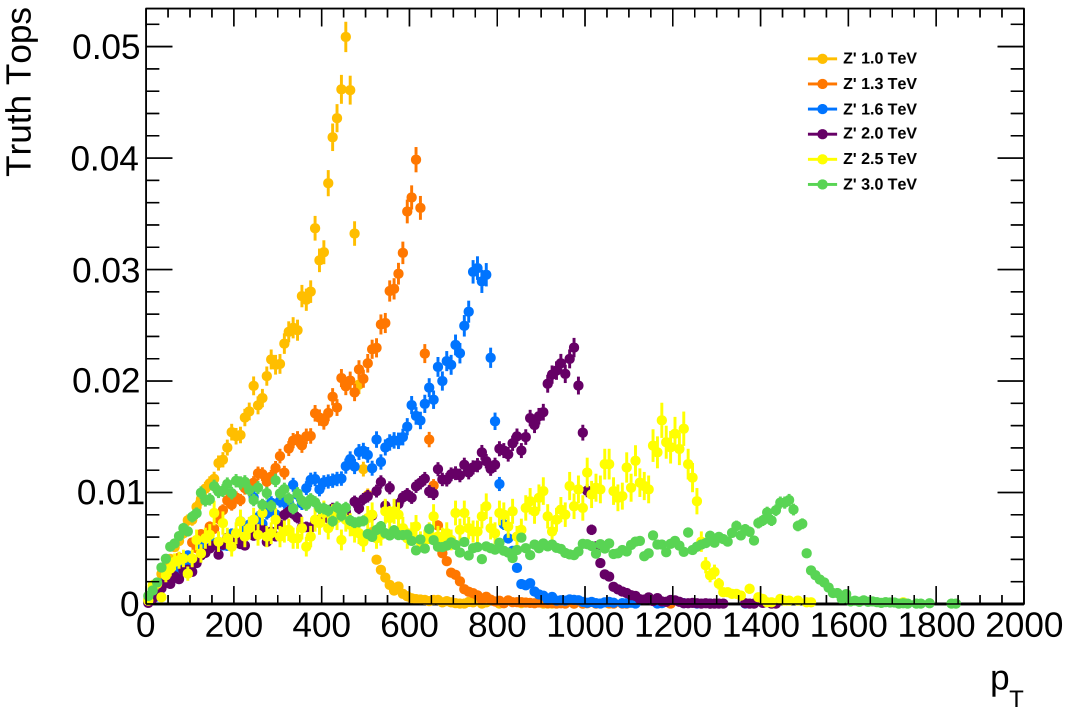

Figure 8.3: The transverse momentum of the top/anti-top quarks in the event for all examined Z' mass points.

collimation are more likely to emerge from particles with higher masses. By requesting the muons be isolated, the ability to probe those higher mass events is diminished.

Another candidate to replace the traditional isolation selection is the so-called mini-isolation. This variable takes into account the strong collimation of the top products with increasing boost. Mini-isolation is defined as the sum of the measured transverse momenta of all tracks in a cone of size of size $\Delta R = k_T/p_T^{\ell}$ around the lepton, where k_T is an adjustable scale and p_T^{ℓ} is the momentum of the lepton in question. This is known as the absolute mini-isolation. This study uses the relative mini-isolation where the absolute value is scaled by the momentum of the lepton (MI/p_T^{ℓ}).

In this analysis the performance of the χ^2_{match} tagger is measured against mini-isolation using a $k_T = 10$ and a lepton is deemed isolated if the p_T in the MI cone is less than 5% that of the lepton. The Muon Tagger operates with the same selection as used in Part 6, the cuts are $|z_0| < 3.0$ mm, $|d_0| < 3.0$ mm and finally $\chi^2_{\text{DoF}} < 3.2$.

Thus two separate selections are applied, one for for mini-isolation and one for SMT.

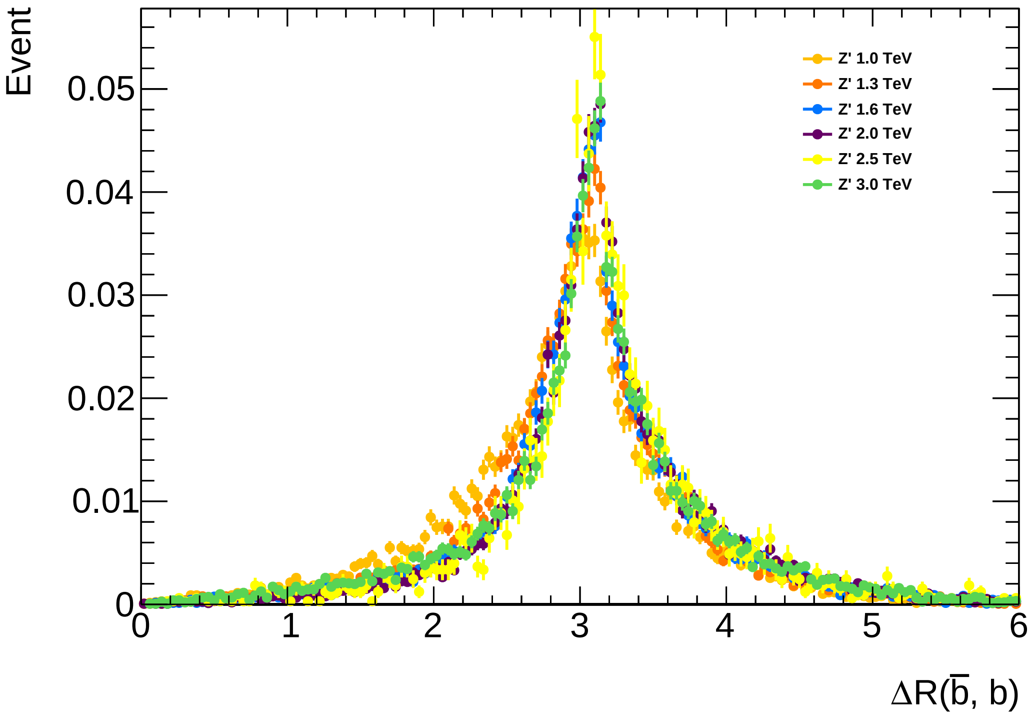

Figure 8.4: The angular separation (ΔR) between the b and $\bar{b}$ in the event for all examined Z' mass points.

Note that both methodologies have different muon reconstruction criteria, these are detailed in Table 8.1.

Table 8.1: Muon reconstruction selection used by Mini-Isolation and by Muon Tagging

Mini-Isolation	Muon-Tagging
MCP Cuts	
$p_{\mathrm{T}} > 20$ GeV	
$\lvert\eta\rvert < 2.5$	
MUID	STACO
$z_0 < 3.0$ mm	Is Combined Muon
IsEM Tight	

The performance of both methodologies are then compared by measuring their efficiency.

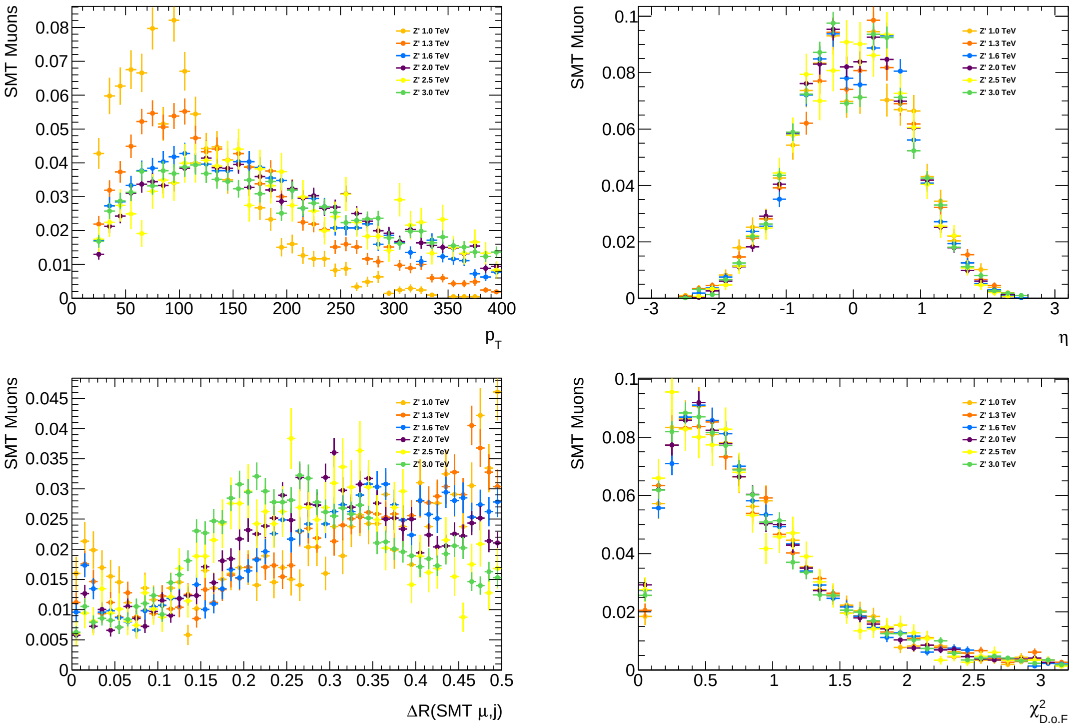

Figure 8.5: This figure shows the distribution of (a) transverse momentum and (b) pseudo-rapidity of muons which pass the SMT selection, the (c) angular separation between those muons and the nearest jet in th event and (d) the χ^2_{match} used in the selection for all tested Z' mass points.

8.4 Efficiency definition

The efficiency measurement was designed to provide an accurate representation of the performance of the soft muon tagger and a valid comparison with mini-isolation. Additional sources of inefficiency such as muon reconstruction are separated out into an additional efficiency which is also quoted. See Fig. 8.7 for a summary of the efficiency measurement.

Firstly, events where a W decays into a muon are selected, this becomes the pool of events from which the efficiency is measured. The selections then diverge and the two sets of reconstruction cuts described in Table 8.1 are applied independently. The efficiency of each sets of reconstruction cuts are measured as:

$$\epsilon_{\mathrm{reco}} = \frac{\text{Muons which pass selection}}{\text{All reconstructed muons}}$$

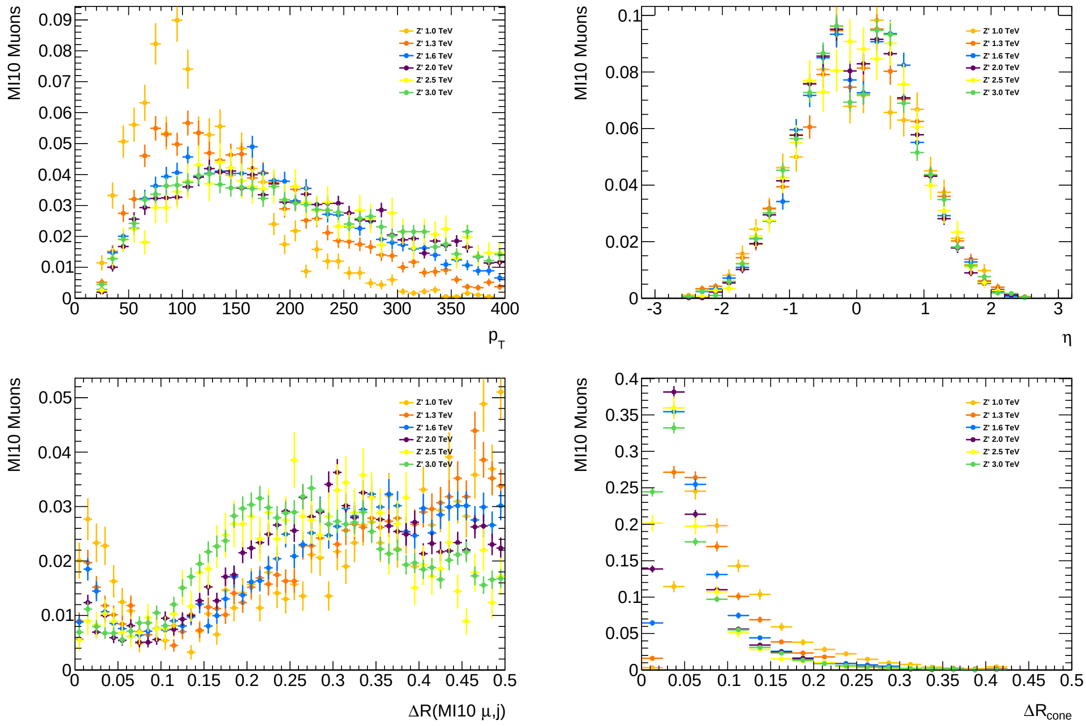

Figure 8.6: This figure shows the (a) transverse momentum and (b) pseudo-rapidity of muons which pass the MI10 selection, the (c) angular separation between those muons and the nearest jet in th event and (d) the cone size used in the selection for all tested Z' mass points.

These good reconstructed muons are then truth-matched to the truth μ from the W if the angular separate (ΔR) between them is less than 0.01. This has an efficiency associated with it, defined as:

$$\epsilon_{\text{match}} = \frac{\text{Muons matched to truth } W \text{ muon}}{\text{Muons which pass selection}}$$

Note that at each stage the denominator is the numerator of the previous efficiency. This allows for a combination of all the efficiencies to obtain an inclusive measure which can used to approximate the number of W muons which would be selected from collision data assuming that the simulation describes the data well.

Next the muons are required to be within $\Delta R < 0.5$ from a jet. The Muon Tagger requires that jets be near a jet, in addition the impetus behind the analysis is to probe highly boosted events exploiting the capabilities of χ^2_{match} tagging. This selection ensures that the muons available for χ^2_{match} tagging are indeed close to a jet. This selection also

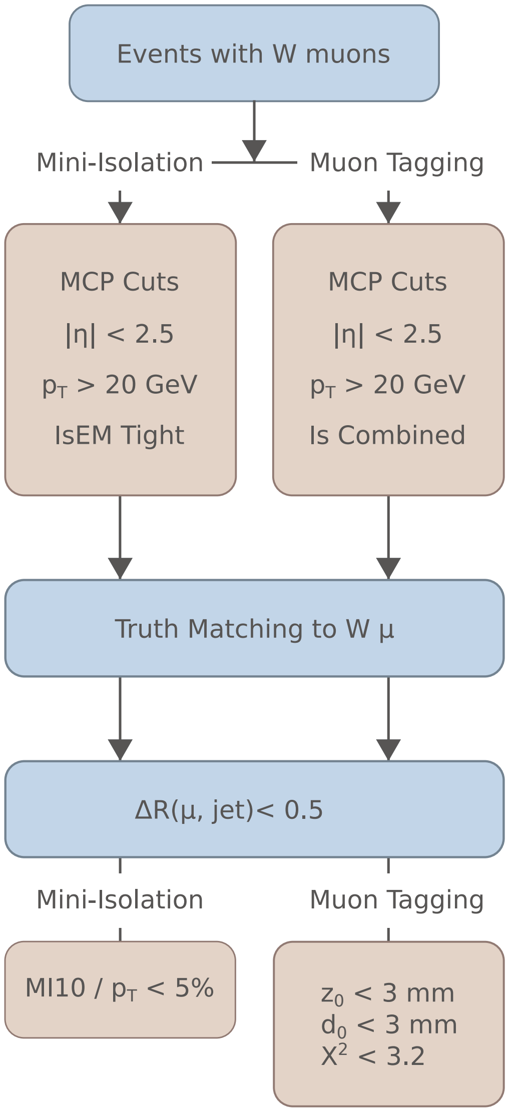

[th!]

Figure 8.7: Structure of the efficiency measurement.

has an efficiency associated with it defined as:

$$\epsilon_{\text{non-iso}} = \frac{\text{Muons with } \Delta\text{R}(\mu, \text{ jet}){<}0.5}{\text{Muons matched to truth } W \text{ muon}}$$

The final step is the application of both the mini-isolation selection and the muon tagging selection discussed a priori. These selections are associated with the final and most interesting sets of efficiencies, defined as:

$$\epsilon_{\text{MT/MI10}} = \frac{\text{Muons which pass MT/MI10 selection}}{\text{Muons with } \Delta\text{R}(\mu, \text{ jet}){<}0.5}$$

Please note that the denominator in every efficiency is a subset of the previous denominator. In other words each selection is applied in sequence and the efficiencies are calculated out of the remaining muons which passed the previous selection criteria.

Note that in the nominal analysis described in [19] muons which are within ΔR of 0.1 of the jet would be removed. The impetus behind the analysis is to exploit the χ^2_{match} tagger to accept additional events where the signal muon emerges very close to the jet axis, thus overlap removal is not part of the χ^2_{match} tagging selection. In order to provide an accurate performance comparison between the χ^2_{match} tagger and mini-isolation, the overlap removal is applied only for the mini-isolation selection at the end of the chain. The additional acceptance gained by using χ^2_{match} tagger is compared to the mini-isolation selection with overlap included:

$$\epsilon = \frac{\text{Muons that pass } \chi^2_{\text{match}} \text{ tagger - MI muons } \Delta \text{ R} < 0.1}{\text{Total } W\ \mu} \tag{8.1}$$

8.5 Results

Mini-isolation is a very efficient method for selecting muons. Table 8.2 shows the efficiency for the χ^2_{match} tagger, mini-isolation and mini-isolation including overlap removal. Across the used mass range, the efficieny of selection remains above 80% and in fact increases with a increased Z' mass. When the Z' has a mass of 3 TeV the efficiency of selection with mini-isolation is 92.5% with no overlap removal. In contrast the efficiency of the χ^2_{match} tagger is more consistent across the used mass range and higher than mini-isolation for a given mass. For a Z' with a mass of 3 TeV the measured efficiency of the χ^2_{match} tagger is 96.2%. When applying the overlap removal the efficiency of mini-isolation falls to 85.0%. As can be seen from Fig. 8.8 the efficiency of mini-isolation dips for muons which are close to a jet however this occurs below the threshold of the overlap removal. Finally the additional acceptance gained as defined in 8.1 is 4.03%. The additional acceptance gained in all mass points is also included in Table 8.2.

Z' Mass [TeV]	χ^2_{match}	MI10	MI10 + Overlap
1.0	94.9%	83.1%	67.0%
1.3	95.8%	89.0%	79.2%
1.6	95.9%	90.4%	81.9%
2.0	96.0%	92.4%	85.7%
2.5	95.8%	92.8%	85.1%
3.0	96.2%	92.5%	85.0%

Table 8.2: Efficiency of selecting a muon by using the χ^2_{match} tagger against mini-isolation. Note that 'MI10 + Overlap' is the efficiency of applying both the mini-isolation cut and overlap removal.

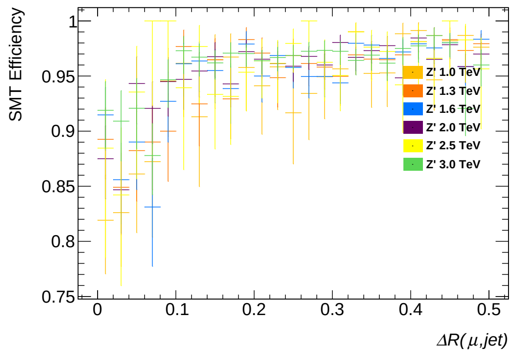

(a) χ^2_{match} muon tagger

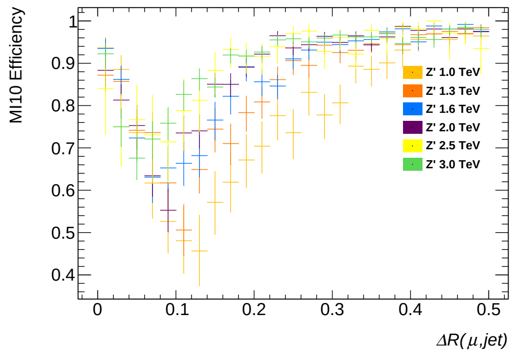

(b) Mini-isolation with $k_T = 10$

Figure 8.8: Efficiency of mini-isolation ($k_T = 10$) and χ^2_{match}muon tagger as a function of the angular separation between the reconstructed muon and the nearest reconstructed jet. Note the dip in the mini-isolation efficiency at low ΔR. In the nominal analysis an overlap removal between the jet and the muon is applied.

8.5.1 Background

A preliminary examination of the amount of background was performed. This was done on the same sample of events but instead of selecting semileptonic events, the all-hadronic events are used as background. While these events do not perfectly mimic the true background, namely $b\bar{b}$, the lack of any real signal muons can provide a suitable preliminary substitute.

The lack of an isolation requirement is expected to result in a substantial increase in the amount of background selected. Additionally the semileptonic b-decays in $b\bar{b}$ would result in muons that the χ^2_{match} tagger will select. The analysis chain described in Section 8.4 is repeated on the same sample used a priori however the truth level selection of events with a W muon is reversed, thus at truth level both W bosons decay

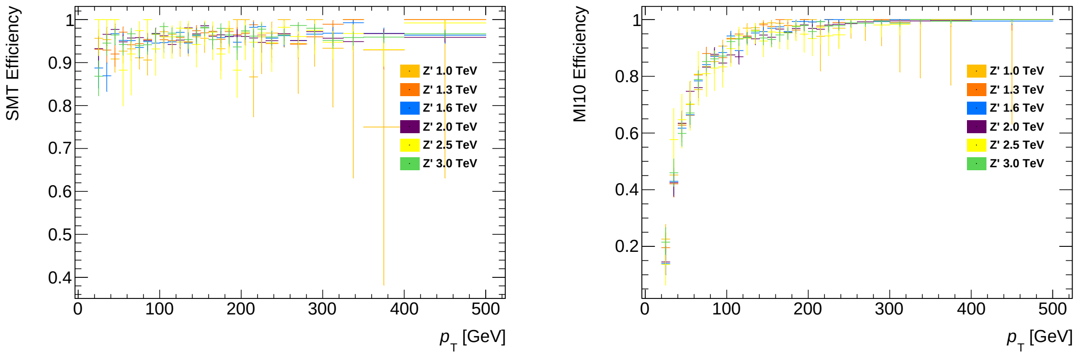

(a) χ^2_{match} muon tagger (b) Mini-isolation with $k_T = 10$

Figure 8.9: Efficiency of mini-isolation ($k_T = 10$) and χ^2_{match}muon tagger as a function of the transverse momentum of the muon.

hadronically.

The results of this selection are presented in Table 8.3. As expected mini-isolation removes a substaintial amount of background while maintaining very high signal efficiency. In comparison, removing the isolation requirement greatly increases the background acceptance when using the χ^2_{match} tagger. A full treatment of the background would be required to account for the background present.

The increase in signal acceptance does not make this methodology sufficiently advantageous particularly when considering the increase in fake rate. An examination of the b-tagging potential of the χ^2_{match} tagger is presented in the next section.

Table 8.3: Fake rate of χ^2_{match} tagger, mini-isolation and mini-isolation including overlap removal as measured using all Z' mass points.

Z' Mass [TeV]	χ^2_{match}	MI10	MI10 + Overlap
1.0	92.8%	4.10%	2.39%
1.3	92.4%	4.77%	3.66%
1.6	91.8%	5.46%	4.55%
2.0	91.1%	7.07%	6.09%
2.5	90.0%	6.40%	5.57%
3.0	90.1%	6.59%	5.68%

8.6 B-tagging potential in boosted events

Table 8.4: caption

Z' Mass [TeV]	Good Muons	Matched Muons	$\Delta R(\mu, jet) < 0.5$	χ^2_{match}-tagged
1.0	16382	9807 (59.8%)	8722 (88.9%)	8237 (94.4%)
1.3	21099	13344 (63.2%)	12083 (90.6%)	11402 (94.4%)
1.6	19947	13012 (65.2%)	11929 (91.7%)	11240 (94.2%)
2.0	23391	15235 (65.1%)	14177 (93.1%)	13276 (93.6%)
2.5	5152	3347 (64.9%)	3137 (93.7%)	2922 (93.1%)
3.0	21766	13835 (63.5%)	13032 (94.2%)	12145 (93.2%)

Chapter 9

Conclusions

Appendices

Appendix A

List of triggers used in calibration

The calibration analysis makes use of an OR of the triggers listed below. The triggers fire based on a set of criteria summarized in the trigger name following the ATLAS trigger naming convention. The list includes generic single low-p_T muon triggers such as `EF_mu6` and `EF_mu15`, single high-p_T muons & jets triggers such as `EF_mu24_j65_a4tchad` and the specialized J/ψ trigger `EF_mu6_Trk_Jpsi_loose`.

- `EF_mu24_j65_a4tchad_EFxe40_tclcw`
- `EF_mu4T_j65_a4tchad_xe60_tclcw_loose`
- `EF_mu24_j65_a4tchad`
- `EF_mu18_tight_e7_medium1`
- `EF_mu4T_j65_a4tchad_xe70_tclcw_veryloose`
- `EF_mu24_j65_a4tchad_EFxe60_tclcw`
- `EF_mu24_tight_b35_mediumEF_j35_a4tchad`
- `EF_mu20i_tight_g5_loose_TauMass`
- `EF_mu6_Trk_Jpsi_loose`
- `EF_mu24i_tight`
- `EF_mu24i_tight_MuonEF`

- EF_mu24i_tight_MG
- EF_mu24i_tight_l2muonSA
- EF_mu24_tight_3j35_a4tchad
- EF_mu24_g20vh_loose
- EF_mu40_MSonly_barrel_tight
- EF_mu50_MSonly_barrel_tight
- EF_mu24_tight_EFxe40
- EF_mu24_tight_L2StarB
- EF_mu18_medium
- EF_mu24_medium
- EF_mu24_tight
- EF_mu24_tight_MuonEF
- EF_mu24_tight_MG
- EF_mu24_tight_L2StarC
- EF_mu36_tight
- EF_mu40_tight
- EF_mu20it_tight
- EF_mu24_g20vh_medium
- EF_mu18_2g10_medium
- EF_mu24_muCombTag_NoEF_tight
- EF_mu10i_loose_g12Tvh_medium
- EF_mu10i_loose_g12Tvh_medium_TauMass

- EF_mu18_2g10_loose
- EF_mu10i_g10_medium_TauMass
- EF_mu20i_tight_g5_medium_TauMass
- EF_mu24_tight_3j45_a4tchad
- EF_mu24_tight_4j45_a4tchad
- EF_mu24_tight_4j35_a4tchad
- EF_mu4T
- EF_mu6
- EF_mu15
- EF_mu40_slow_tight
- EF_mu60_slow_tight1
- EF_mu22_IDTrkNoCut_tight
- EF_mu8_4j45_a4tchad_L2FS
- EF_mu6_Trk_Jpsi_loose_L2StarB
- EF_mu6_Trk_Jpsi_loose_L2StarA
- EF_mu24_j65_a4tchad_EFxe40wMu_tclcw
- EF_mu24_j65_a4tchad_EFxe60wMu_tclcw
- EF_mu6T_2b55_medium_2j55_a4tchad_L1J20_matched
- EF_mu24i_tight_muFast
- EF_mu4T_L2StarB
- EF_mu6_L2StarB
- EF_mu15_vbf_L1TAU8_MU10

Appendix B

List of combined muon performance (MCP) cuts

Bibliography

[1] J. Beringer et al. (Particle Data Group). The Review of Particle Physics. *Physical Review D*, 86:010001+, 2012.

[2] B. Odom, D. Hanneke, B. D'Urso, and G. Gabrielse. New measurement of the electron magnetic moment using a one-electron quantum cyclotron. *Phys. Rev. Lett.*, 97:030801, Jul 2006.

[3] et. al. G. Aad. Observation of a new particle in the search for the standard model higgs boson with the {ATLAS} detector at the {LHC}. *Physics Letters B*, 716(1):1 – 29, 2012.

[4] Serguei Chatrchyan et al. Observation of a new boson at a mass of 125 GeV with the CMS experiment at the LHC. *Phys.Lett.*, B716:30–61, 2012.

[5] D.H. Perkins. *Introduction to High Energy Physics.* Cambridge University Press, 2000.

[6] D. Griffiths. *Introcution to Elementary Particles.* "John Wiley & Sons, Inc", 1987.

[7] Nicola Cabibbo. Unitary symmetry and leptonic decays. *Phys. Rev. Lett.*, 10:531–533, Jun 1963.

[8] Makoto Kobayashi and Toshihide Maskawa. Cp-violation in the renormalizable theory of weak interaction. *Progress of Theoretical Physics*, 49(2):652–657, 1973.

[9] Lincoln Wolfenstein. Parametrization of the kobayashi-maskawa matrix. *Phys. Rev. Lett.*, 51:1945–1947, Nov 1983.

[10] S. W. Herb, D. C. Hom, L. M. Lederman, J. C. Sens, H. D. Snyder, J. K. Yoh, J. A. Appel, B. C. Brown, C. N. Brown, W. R. Innes, K. Ueno, T. Yamanouchi, A. S. Ito, H. Jöstlein, D. M. Kaplan, and R. D. Kephart. Observation of a dimuon resonance at 9.5 gev in 400-gev proton-nucleus collisions. *Phys. Rev. Lett.*, 39:252–255, Aug 1977.

[11] CDF Collaboration. Observation of top quark production in $p\bar{p}$ collisions with the collider detector at fermilab. *Phys. Rev. Lett.*, 74:2626–2631, Apr 1995.

[12] D0 Collaboration. Search for high mass top quark production in $p\bar{p}$ collisions at $\sqrt{s}$=1.8 tev. *Phys. Rev. Lett.*, 74:2422–2426, Mar 1995.

[13] Johann H. Kuhn, A. Reiter, and Peter M. Zerwas. Z Decays to Top Quarks. *Nucl.Phys.*, B272:560, 1986.

[14] O.W. Greenberg. CPT violation implies violation of Lorentz invariance. *Phys.Rev.Lett.*, 89:231602, 2002.

[15] Georges Aad et al. Measurement of the mass difference between top and anti-top quarks in pp collisions at $\sqrt(s) = 7$ TeV using the ATLAS detector. *Phys.Lett.*, B728:363–379, 2014.

[16] Serguei Chatrchyan et al. Measurement of the mass difference between top and antitop quarks. *JHEP*, 1206:109, 2012.

[17] Georges Aad et al. Measurement of the top quark pair production charge asymmetry in proton-proton collisions at $\sqrt{s} = 7$ TeV using the ATLAS detector. *JHEP*, 1402:107, 2014.

[18] Serguei Chatrchyan et al. Measurements of the $t\bar{t}$ charge asymmetry using the dilepton decay channel in pp collisions at $\sqrt{s} = 7$ TeV. 2014.

[19] Georges Aad et al. Search for $t\bar{t}$ resonances in the lepton plus jets final state with ATLAS using 4.7 fb^{-1} of pp collisions at $\sqrt{s} = 7$ TeV. *Phys.Rev.*, D88(1):012004, 2013.

[20] A search for $t\bar{t}$ resonances in the lepton plus jets final state with ATLAS using 14 fb^{1} of pp collisions at $\sqrt{s} = 8$ TeV. Technical Report ATLAS-CONF-2013-052, CERN, Geneva, May 2013. Not published in the proceedings.

[21] Serguei Chatrchyan et al. Search for Z' resonances decaying to $t\bar{t}$ in dilepton+jets final states in pp collisions at $\sqrt{s} = 7$ TeV. *Phys.Rev.*, D87:072002, 2013.

[22] Serguei Chatrchyan et al. Search for anomalous $t\bar{t}$ production in the highly-boosted all-hadronic final state. *JHEP*, 1209:029, 2012.

[23] The CMS Collaboration. Search for $t\bar{t}$ resonances in semileptonic final state. Technical Report CMS-PAS-B2G-12-006, CERN, Geneva, 2013.